J. Fluid Mech. (2021), *vol*. 928, A10, doi:10.1017/jfm.2021.818

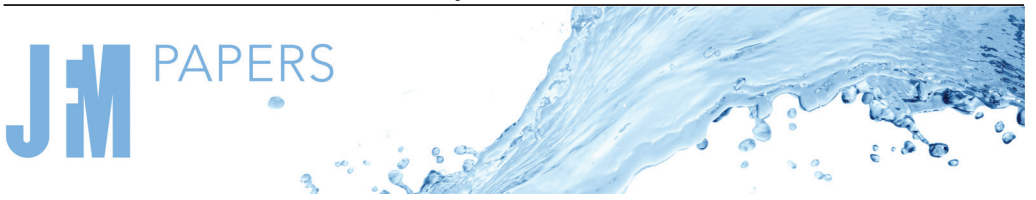

Statistical characteristics of turbulent mixing in spherical and cylindrical converging Richtmyer–Meshkov instabilities

Xinliang Li[1,2], Yaowei Fu[1,2], Changping Yu[1,2,†] and Li Li[3,†]

[1]LHD, Institute of Mechanics, Chinese Academy of Sciences, Beijing 100190, PR China

[2]School of Engineering Science, University of Chinese Academy of Sciences, Beijing 100049, PR China

[3]Institute of Applied Physics and Computational Mathematics, Beijing 100094, PR China

(Received 10 November 2020; revised 4 September 2021; accepted 16 September 2021)

In this paper, the Richtmyer–Meshkov instabilities in spherical and cylindrical converging geometries with a Mach number of approximately 1.5 are investigated by using the high resolution implicit large eddy simulation method, and the influence of the geometric effect on the turbulent mixing is investigated. The heavy fluid is sulphur hexafluoride (SF6), and the light fluid is nitrogen (N2). The shock wave converges from the heavy fluid into the light fluid. The Atwood number is 0.678. The total structured and uniform Cartesian grid node number in the main computational domain is 2048^3. In addition, to avoid the influence of boundary reflection, a sufficiently long sponge layer with 50 non-uniform coarse grids is added for each non-periodic boundary. Present numerical simulations have high and nonlinear initial perturbation levels, which rapidly lead to turbulent mixing in the mixing layers. Firstly, some physical-variable mean profiles, including mass fraction, Taylor Reynolds number, turbulent kinetic energy, enstrophy and helicity, are provided. Second, the mixing characteristics in the spherical and cylindrical turbulent mixing layers are investigated, such as molecular mixing fraction, efficiency Atwood number, turbulent mass-flux velocity and density self-correlation. Then, Reynolds stress and anisotropy are also investigated. Finally, the radial velocity, velocity divergence and enstrophy in the spherical and cylindrical turbulent mixing layers are studied using the method of conditional statistical analysis. Present numerical results show that the geometric effect has a great influence on the converging Richtmyer–Meshkov instability mixing layers.

Key words: compressible turbulence, shock waves, turbulent mixing

† Email addresses for correspondence: cpyu@imech.ac.cn, li_li@iapcm.ac.cn

1. Introduction

The Richtmyer–Meshkov instability (RMI) will occur if a shock wave passes through a perturbed interface between different materials. The main cause of RMI is baroclinic instability ($\nabla P \cdot \nabla \rho \neq 0$), which will result in the deposition of baroclinic vorticity on the perturbed interface. Under the action of baroclinic vorticity, the amplitude of perturbation experiences linear and nonlinear growth, and then leads to turbulent mixing.

Research on RMI began in the 1950s. This phenomenon was first discovered by Markstein (1957), and then Richtmyer (1960), by reference to the analytical method of Rayleigh–Taylor instability (RTI) (Rayleigh 1883; Taylor 1950), first carried out a theoretical study on a small sinusoidal single-mode wrinkled interface accelerated by a plane shock and proposed an impulsive model for the growth of amplitude of perturbation. Later, Meshkov's (1969) shock tube experiment verified the accuracy of Richtmyer's theoretical model to some extent. The RMI can be considered as a RTI of pulsed acceleration; however, different from RTI, RMI will develops no matter whether the shock wave converges from a heavy fluid into light fluid or from a light fluid into heavy fluid, although the development process of the perturbed interface is greatly different in these two cases. If the shock wave is incident from a heavy fluid into a light fluid, the baroclinic vorticity deposited on the interface will first make the amplitude of the perturbed interface decrease gradually and then increase in inverse, which is the so-called phase inversion phenomenon (Zhai *et al.* 2019). If the shock wave is incident from a light fluid into a heavy fluid, the baroclinic vorticity deposited on the interface will increase the amplitude of the perturbed interface continuously. The RMI is very important in nature and many practical engineering applications, such as inertial confinement fusion (ICF), supernova explosion and supersonic combustion (Brouillette 2002; Livescu 2020). For example, in ICF, RMI will induce turbulent mixing between the fuel and ablative layer in the capsule, which can further influence the compression of the capsule and the formation of the hot spot in the centre, leading to the failure of ignition. In supernova explosion, when the shock wave caused by the outward projectile of matter converges toward the centre and passes through the interface between different density materials, the RMI is induced and then affects the life evolution of stars. In a supersonic combustion, the shock wave interacts with the interface of fuel and oxidant and accelerates the mixing between fuel and oxidant, which is helpful to the combustion process.

Very excellent review work for interfacial instability has been done by Zhou (2017*a*,*b*) and Zhou *et al.* (2019, 2021). From these papers, it can be found that most of previous theoretical, experimental and numerical studies on RMI have focused on the case of a plane shock interacting with a perturbed plane interface (Chapman & Jacobs 2006; Tritschler *et al.* 2014; Liu & Xiao 2016; Zhou, Cabot & Thornber 2016; Reese *et al.* 2018; Liang *et al.* 2019, 2020*a*,*b*; Luo *et al.* 2019*b*; Hill & Abarzhi 2020; Liu *et al.* 2020; Sun *et al.* 2020*a*; Zhao, Xia & Cao 2020; Peng *et al.* 2021). However, in nature and many practical engineering applications, almost all RMI are converging, such as the cylindrical converging shock wave interacting with a cylindrical interface or the spherical converging shock wave interacting with a spherical interface. Moreover, comparing with the plane RMI, the flow development of converging RMI is more intractable because of the influence of the Bell–Plesset (BP) effect (Bell 1951; Plesset 1954; Epstein 2004), stronger compressibility and the Rayleigh–Taylor (RT) effect.

Using a Lagrange-remap code TURMOIL, Youngs & Williams (2008) simulated turbulent mixing in a sector of spherical implosions with random amplitude perturbations that were initially applied to the interface between light and heavy fluids. The authors

found that the width of the mixing layer shrank slightly and the sub-grid dissipation was close to being mesh converged as the mesh was refined. Referring to Youngs and Williams' problem description, Boureima, Ramaprabhu & Attal (2018) used the astrophysical FLASH code to carry out numerical simulations for spherical implosion of relevance to the ICF application. Boureima *et al*.'s numerical results showed that the radial trajectory of the undisturbed interface and the width of turbulent mixing layer to be in very good agreement with the results of Youngs and Williams. Boureima *et al*. argued that the spherical implosion was susceptible to multiple factors, including RMI, RTI, BP effect and anisotropy.

El Rafei *et al.* (2019) conducted three different large eddy simulations (LES) in spherical coordinates to investigate the effects of different initial surface perturbations on the turbulent mixing in spherical implosion, and found that the initial perturbations had almost no effect on the high wavenumber shape of the spectrum. For all three cases, the spectra exhibit an approximate $-5/3$ spectral slope. However, for the initial broadband perturbation case, the low wavenumber portion of the spectrum was still influenced. Lombardini (2008) and Lombardini & Pullin (2009) investigated the characteristics of turbulence and mixing in cylindrical converging RMI theoretically and numerically, and compared with the results of plane RMI. A simple but more complete model for the asymptotic growth of a three-dimensional cylindrical converging RMI mixing layer was proposed by Lombardini. Lombardini's LES results showed that the growth of the cylindrical mixing layer lasted longer than the plane RMI mixing layer. Independent of the incident Mach number, the cylindrical turbulent mixing layer in the late time was weakly compressible. The mixing efficiency was greater for high incident Mach number. Isotropy for Kolmogorov directional microscales and anisotropy for velocity power spectra were found. The probability density function of the mixture fraction in the cylindrical mixing layer showed a weak bimodal characteristic. Similar to the plane RMI, a $-5/3$ scaling law was observed for the turbulent kinetic energy after the reshock. Subsequently, Lombardini *et al.* (2014*a*,*b*) conducted LES for the spherical converging RMI with spherical harmonic function disturbance. In the spherical mixing layer, the turbulent mixing exhibited stronger anisotropy at large scales than that at small scales and the inertial sub-region of kinetic energy and density spectra also showed a Kolmogorov-like $-5/3$ scaling law in late time, which indicated that the turbulent scales were rarely affected by the spherical mixing layer curvature. By numerically simulating two-dimensional single-mode interfaces driven by convergent shock waves, Tang *et al.* (2021) investigated the effects of the Atwood number on the compressibility, RT stabilization and the nonlinearity.

The linear stabilities of spherical and cylindrical converging RTI/RMI in an arbitrary number of stratified shells had been studied by Mikaelian (1990, 2005). In these two papers, the evolution equations of interfacial perturbations for stratified spherical and cylindrical shells were derived. Subsequently, Liu, He & Yu (2012) presented a simple method based on the formal perturbation expansion and potential flow theory to investigate the cylindrical effects in weakly nonlinear RMI by considering the nonlinear correlations up to fourth order. Then, based on the Padé approximation and perturbation expansion directly on the perturbed interface, Liu *et al.* (2014) developed a nonlinear theory to describe the cylindrical RMI under incompressible, inviscid and irrotational assumptions, and obtained the fourth-order explicit solution in the weakly nonlinear region. Later, using weakly nonlinear analysis up to the third order, Liu *et al.* (2018) researched the finite-thickness effect on harmonics in the RMI for arbitrary Atwood number and found that the thickness had a large effect on the amplitude of the first three harmonics.

Experimental investigations of cylindrical converging RMI in shock tubes had been conducted by several researchers, such as Hosseini & Takayama (2005), Biamino *et al.* (2015), Luo *et al.* (2015, 2018, 2019*a*), Zhai *et al.* (2017), Rodriguez *et al.* (2017), Ding *et al.* (2017, 2019), Lei *et al.* (2017), Li *et al.* (2020), Vandenboomgaerde *et al.* (2018), Courtiaud *et al.* (2019), Sun *et al.* (2020*b*) and Zou *et al.* (2019). These experimental results are particularly helpful for the development of theory and numerical simulation. However, to the author's knowledge, there are few experiments on the spherical converging RMI. Inspired by this, we plan to investigate the similarities and differences between the spherical and cylindrical converging RMI using the method of high resolution implicit large eddy simulation (ILES).

In our previous paper (Fu, Yu & Li 2020), the turbulent kinetic energy and enstrophy transport equations in the mixing layers of spherical and cylindrical converging RMI were analysed and compared in detail. In the present paper, the main focus is on the statistical characteristics of turbulence and mixing in spherical and cylindrical converging RMI mixing layers. Therefore, two numerical simulations are conducted, using the high accuracy finite difference solver code named *Opencfd-Comb* developed by our group for multicomponent and chemical reaction flows, for the spherical and cylindrical converging RMI with a Mach number of approximately 1.5. The heavy fluid is SF6, and the light fluid is N2. The shock waves converge from the heavy fluids into the light fluids. The Atwood numbers are both $A = (\rho_h - \rho_l)/(\rho_h + \rho_l) = 0.678$. Here, ρ_h is the density of SF6 and ρ_l is the density of N2 at the initial time.

2. Computational set-up and numerical method

In this paper, three-dimensional compressible and multicomponent Navier–Stokes (NS) equations without chemical reaction, including the mass conservation equation, momentum conservation equation, energy conservation equation and species conservation equation, are solved in the Cartesian coordinate system using the finite difference method. The NS equations are as follows:

$$\frac{\partial \rho}{\partial t} + \frac{\partial (\rho u_i)}{\partial x_i} = 0, \tag{2.1}$$

$$\frac{\partial (\rho u_i)}{\partial t} + \frac{\partial (\rho u_i u_j)}{\partial x_j} = \frac{-\partial P}{\partial x_i} + \frac{\partial \tau_{ij}}{\partial x_j}, \tag{2.2}$$

$$\frac{\partial E}{\partial t} + \frac{\partial [(E+P)u_j]}{\partial x_j} = \frac{\partial [u_i \tau_{ij} + q_j]}{\partial x_j}, \tag{2.3}$$

$$\frac{\partial \rho_k}{\partial t} + \frac{\partial (\rho_k u_i)}{\partial x_i} = \frac{\partial}{\partial x_i}\left[\rho D_{km} \frac{\partial Y_k}{\partial x_i}\right], \tag{2.4}$$

where t denotes the time, x_i denotes the spatial position in the i direction, u_i denotes the velocity in the i direction, P denotes the static pressure, $E = \rho(e + u_i u_i/2)$ denotes the total energy per unit volume where e is the internal energy per unit mass, ρ denotes the density of the mixture, ρ_k denotes the density of species k, $Y_k = \rho_k/\rho$ is the mass fraction of species k, D_{km} denotes the mixture diffusion coefficient of species k, τ_{ij} denotes the viscous stress tensor and q_j denotes the heat flux in the j direction. According to the Newtonian fluid hypothesis, the viscous stress tensor is calculated using the equation,

$$\tau_{ij} = \mu\left(\frac{\partial u_i}{\partial x_j} + \frac{\partial u_j}{\partial x_i} - \frac{2}{3}\delta_{ij}\frac{\partial u_k}{\partial x_k}\right), \tag{2.5}$$

where μ is the viscosity coefficient of the mixture and δ_{ij} is the Kronecker function. The heat flux can be obtained by using Fourier's law of heat conduction

$$q_j = \lambda \frac{\partial T}{\partial x_j} + \rho \sum_k D_{km} h_k \frac{\partial Y_k}{\partial x_k}, \tag{2.6}$$

where λ denotes the thermal conductivity coefficient of the mixture, $h_k = C_{pk}T$ denotes the enthalpy per unit mass of species k, T denotes the temperature of the mixture, $C_{pk} = \gamma_k R_k/(\gamma_k - 1)$ denotes the specific heat at constant pressure of species k, γ_k and $R_k = R_0/W_k$ denote the specific heat ratio and gas constant of species k, respectively. Here, R_0 is the universal gas constant and W_k is the molecular weight of species k. In the present numerical simulations, it is assumed that the N2 and SF6 both are calorically perfect gas with $\gamma_{N2} = 1.4$ and $\gamma_{SF6} = 1.09$.

The viscosity and thermal conductivity coefficients of species k can be computed by using the polynomial fit method used in the *CHEMKIN* software (Design 2008)

$$\ln \mu_k = \sum_{n=1}^{N} b_{n,k} (\ln T)^{n-1}, \tag{2.7}$$

$$\ln \lambda_k = \sum_{n=1}^{N} c_{n,k} (\ln T)^{n-1}. \tag{2.8}$$

These coefficients of polynomial fit can be found in Appendix A. The viscosity and thermal conductivity coefficients of the mixture can be calculated by using the Wilke formula (1950),

$$\mu = \sum_{k=1}^{N} \frac{X_k \mu_k}{\sum_{j=1}^{N} X_j \phi_{kj}}, \tag{2.9}$$

$$\phi_{kj} = \frac{1}{\sqrt{8}} \left(1 + \frac{W_k}{W_j}\right)^{-1/2} \left(1 + \left(\frac{W_j}{W_k}\right)^{1/4} \left(\frac{\mu_k}{\mu_j}\right)^{1/4}\right)^2, \tag{2.10}$$

$$\lambda = \frac{1}{2} \left(\sum_{k=1}^{N} X_k \lambda_k + \frac{1}{\sum_{k=1}^{N} X_k \lambda_k} \right), \tag{2.11}$$

where X_k denotes the volume fraction. In addition, the mixture diffusion coefficient of species k is obtained by using the Schmidt number $Sc_k = \mu/\rho D_{km}$ and the Schmidt numbers of N2 and SF6 both are assumed to be 1 (Tritschler *et al.* 2014).

For the initial material interface, in order to make sure that there is no singularity on the spherical surface, the spherical harmonic function is used to generate the initial perturbation

$$\psi(r, \theta, \varphi) = \frac{1}{2} \left\{ 1 - \tanh \left[\frac{r - \xi_0(\theta, \varphi)}{L_r} \right] \right\}, \tag{2.12}$$

$$\xi_0(\theta, \varphi) = R_0 - a_0 |f(R_0, \theta, \varphi)|, \tag{2.13}$$

$$f(R_0, \theta, \varphi) = \sum_{l=0}^{N} \sum_{m=-l}^{l} f_{lm} Y_{lm}(\theta, \varphi), \tag{2.14}$$

$$f_{lm} = \sqrt{(2l+1)C_l} \frac{\cos(2\pi\omega_l^m)}{\sqrt{\sum_{i=-l}^{l} \cos(2\pi\omega_l^i)^2}}, \tag{2.15}$$

$$C_l = \frac{1}{4(2l_0+1)} \frac{1}{\sigma_0\sqrt{2\pi}} exp\left[-\frac{(l-l_0)^2}{2\sigma_0^2}\right], \tag{2.16}$$

where ω_l^m is a series of random numbers distributed between 0 and 1, and these random numbers are the same for different numerical simulations in this paper. The mass fraction of light fluid near the material interface is $Y_{\mathrm{N2}} = \psi$ and $Y_{lm}(\theta, \varphi)$ is the spherical harmonic function defined as follows:

$$Y_{lm} = (-1)^m \sqrt{\frac{(2l+1)}{4\pi} \frac{(l-|m|)!}{(l+|m|)!}} P_l^m(\cos\theta)\, \mathrm{e}^{\mathrm{i}m\varphi}. \tag{2.17}$$

Here, $P_l^m(x)$ denotes the associated Legendre polynomial and is written as

$$P_l^m(x) = (1-x^2)^{|m|/2} \frac{\mathrm{d}^{|m|}}{\mathrm{d}x^{|m|}} P_l(x). \tag{2.18}$$

Here, $P_l(x)$ is the l-order Legendre polynomial and defined as,

$$P_l(x) = \frac{1}{2^l l!} \frac{\mathrm{d}^l}{\mathrm{d}x^l} (x^2-1)^l. \tag{2.19}$$

For the simulation of cylindrical converging RMI, $r = \sqrt{x^2+y^2}$, $\varphi = a\tan 2(y, x)$ and $\theta = \pi(k-1)/(n_k-1)$. Here, n_k is the grid node number in the spanwise direction. For the simulation of spherical converging RMI, $r = \sqrt{x^2+y^2+z^2}$, $\varphi = a\tan 2(z, x)$ and $\theta = a\tan 2(\sqrt{x^2+z^2}, y)$. The radius of the N2 density layer at the initial time is $R_0 = 7$ mm. In addition, $a_0 = 0.375$ mm, $L_r = 0.2$ mm, $N = 40$, $l_0 = 20$, $\sigma_0 = l_0/15$ and the position of shock wave at the initial time is located at $R_{sp} = 8.5$ mm. The present numerical simulations have high initial perturbation levels, which rapidly lead to turbulent mixing in the mixing layers. In the present paper, we plan to study the influence of the geometric effect on the turbulent mixing, but it is impossible to make the initial perturbation exactly the same on different geometric surfaces. The cylindrical initial condition is a remapping of the same perturbation as in the spherical case. The smearing effect of the cylindrical initial condition can be gradually reduced by gradually reducing the statistical region towards the middle. Statistical averaging is done over the whole mixing layer. We will evaluate the effects of different statistical regions in more detail in future work. The main computational domains in the Cartesian coordinate system for spherical and cylindrical converging RMI both are $L_x = L_y = L_z = L = 20$ mm.

In addition, in order to avoid the influence of boundary reflection, a sufficiently long sponge layer of approximately $40L$ with 50 non-uniform coarse grid nodes is added for each non-periodic boundary. The flow parameters at the initial time can been seen in table 1. The isosurface of $Y_{\mathrm{SF6}} = 0.99$ for spherical and cylindrical converging RMI and

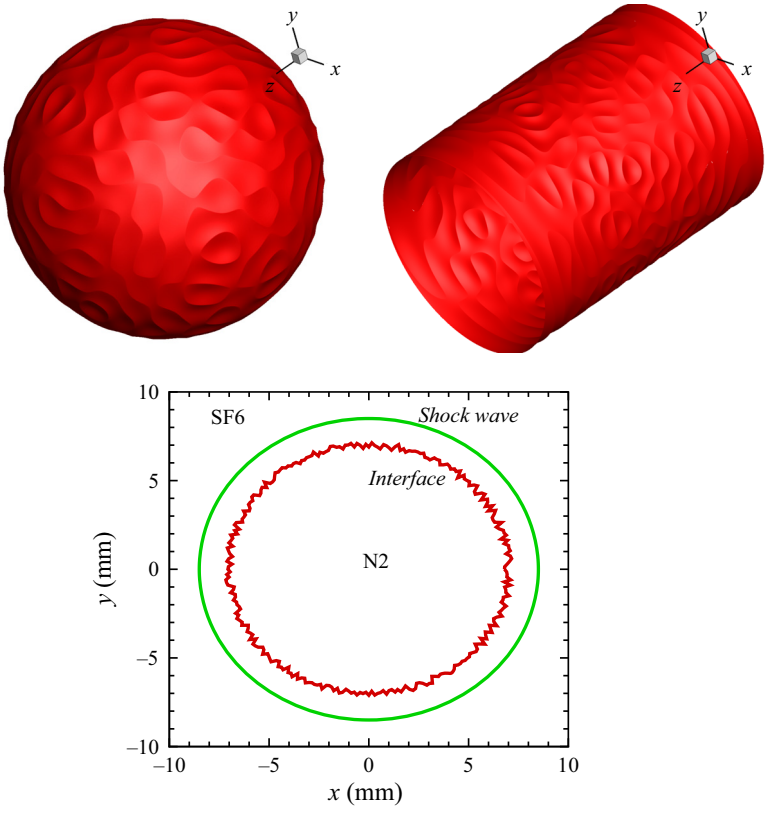

Figure 1. Isosurfaces of $Y_{SF6} = 0.99$ for spherical and cylindrical converging RMI, and the shock wave and interface configuration diagram at the initial time.

	Pre-shock		Post-shock
	N2	SF6	SF6
P/pa	101325	101325	233435.425
$\rho/(\mathrm{kg\ m^{-3}})$	1.145	5.971	12.748
$U_r/(\mathrm{m\ s^{-1}})$	0	0	108.456
γ	1.4	1.09	1.09

Table 1. Flow parameters at the initial time. Here, U_r is radial velocity.

the shock wave and interface configuration diagram at the initial time are displayed in figure 1.

When solving the NS equations by using the finite difference method, the sixth-order monotonicity-preserving optimized scheme (OMP6) (Li, Leng & He 2013) is used to discretize the convective terms. An eighth-order central difference scheme is employed for the viscous terms and a third-order Runge–Kutta approach is adopted for the time integration.

In order to ensure the mesh convergence, four sets of grids are selected for the simulations of cylindrical and spherical converging RMI. The grid node numbers in the

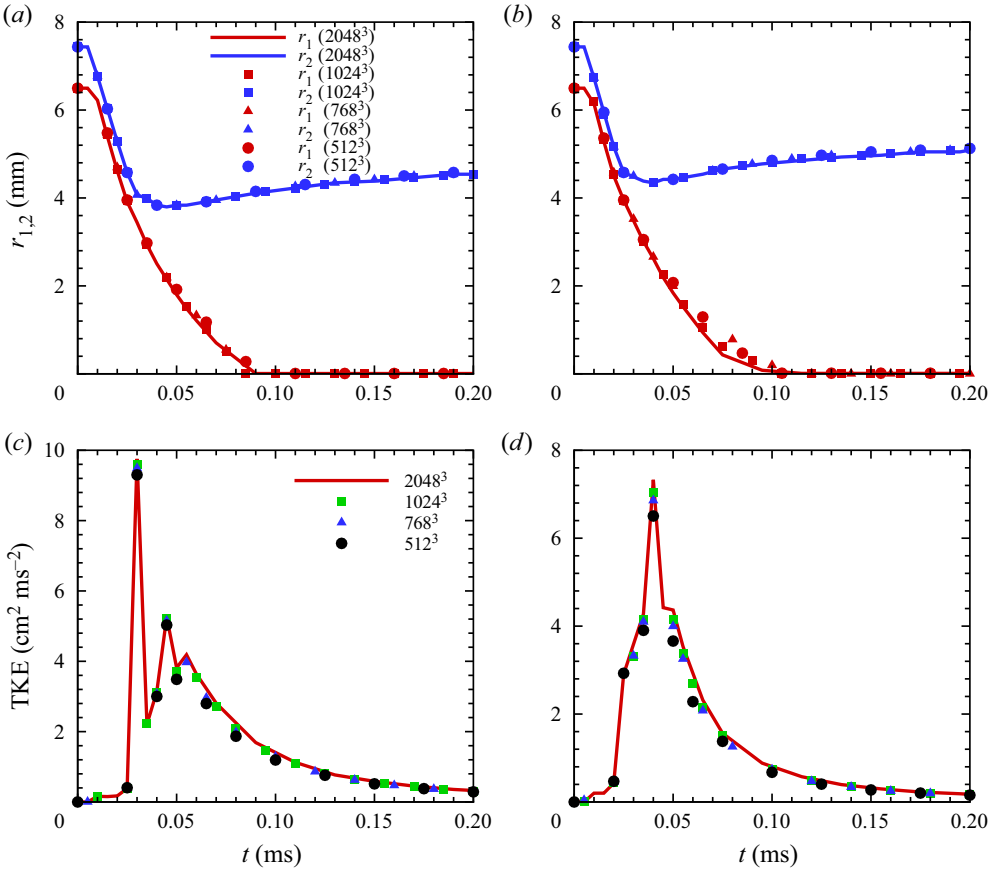

Figure 2. Inner and outer radii of mixing layer (*a*,*b*) and turbulent kinetic energy (*c*,*d*) vs. time. Here, (*a*,*c*) are for cylindrical converging RMI and (*b*,*d*) are for spherical converging RMI.

main computational domain are 512^3, 768^3, 1024^3 and 2048^3, respectively. Therefore, the maximum total grid node number is $2148^2 \times 2048$ for a cylindrical converging RMI and 2148^3 for a spherical converging RMI. In addition, in the following paper, the spherical or cylindrical shell averaging method is used to process the data of the simulations. In the time evolution analysis, the physical quantities are averaged in the entire spherical or cylindrical mixing layer.

Figures 2(*a*)–2(*d*) respectively show the time developments of the inner and outer radii of the mixing layers and the turbulent kinetic energy in the mixing layers for cylindrical and spherical converging RMI obtained from four sets of grids. Here, the mixing layer width is defined by using the threshold of mass fraction. The inner radius r_1 is the position where the mass fraction of heavy fluid is 0.01. The outer radius r_2 is the position where the mass fraction of light fluid is 0.01. It can be seen that the outer radii are identical for four sets of grids. However, there are some very small differences for the inner radii when the inner radii are near the converging centres. The main reason is that, when the shell averaging method is used, the grid node number is relatively small near the converging centre position. For turbulent kinetic energy, each peak indicates that the transmitted or reflected shock wave is passing through the mixing layer. Therefore, there are some slight

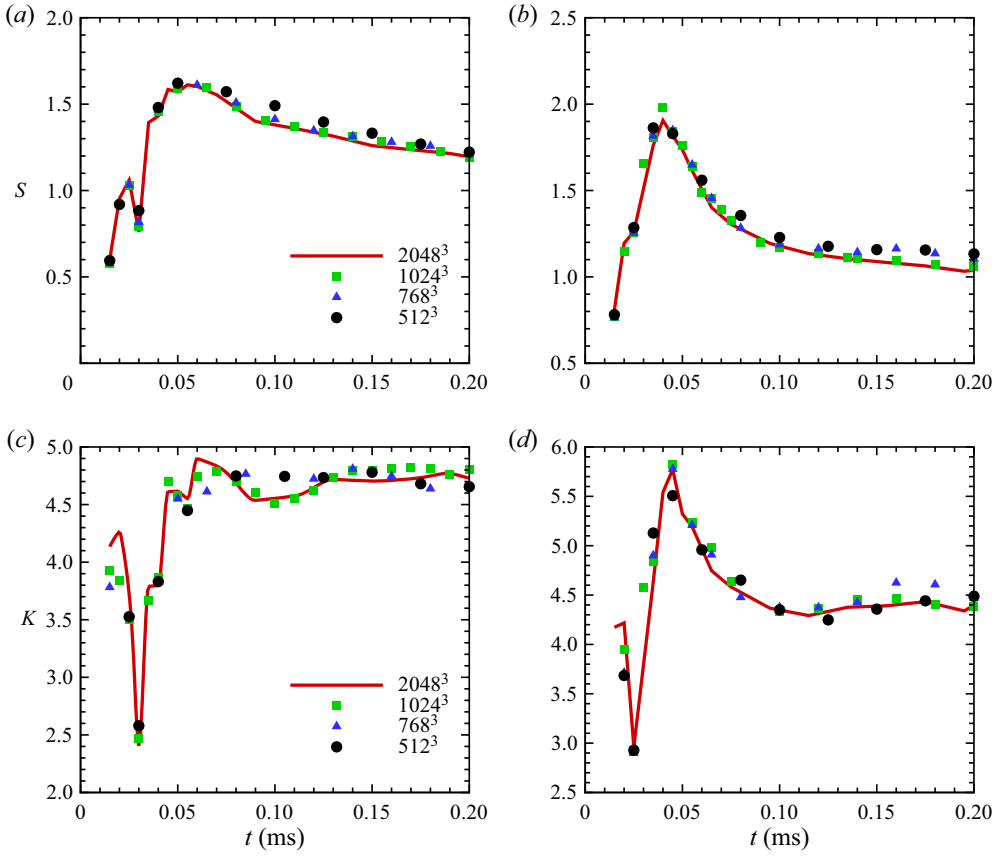

Figure 3. Skewness (*a*,*b*) and kurtosis factors (*c*,*d*) vs. time. Here, (*a*,*c*) are for cylindrical converging RMI and (*b*,*d*) are for spherical converging RMI.

differences at the peak positions due to numerical dissipation. At other times, the turbulent kinetic energy is exactly the same.

Figures 3(*a*)–3(*d*) show the time developments of the skewness and kurtosis factors in cylindrical and spherical mixing layers. The skewness factor is a third-order moment and is defined as $S = \langle u''^3 \rangle / \langle u''^2 \rangle^{3/2}$. Similarly, the kurtosis factor is a fourth-order moment and is defined as $K = \langle u''^4 \rangle / \langle u''^2 \rangle^2$. Here u_i'' is the density-weighted radial fluctuation velocity. It can be seen from figure 3 that both the skewness factor and the kurtosis factor have achieved grid convergence.

Because we use a monotonicity-preserving and dissipative numerical scheme in these numerical simulations, and the numerical results achieve at least fourth-order statistical convergence, we believe that the current numerical simulations meet the requirements of ILES. In addition, it is worth noting that most of the turbulence and mixing statistics in the subsequent analysis of the present paper are of first-order or second-order statistics. In order to ensure the reliability of our numerical simulations, the results on the finest grid are used for subsequent analysis.

3. Results and discussions

In terms of the RMI and RTI, the evolution of turbulent mixing can be characterized on three different levels, i.e. mixing layer width, mean profiles and turbulent fluctuation

statistics (Zhang *et al.* 2020*a*,*b*). In this section, a comprehensive analysis will be conducted for the spherical and cylindrical converging RMI on these three different levels.

First of all, the isosurfaces of mass fractions of SF6 for spherical and cylindrical converging RMI at different moments are displayed in figures 4 and 5, respectively. In order to observe the degree of mixing between species, only one eighth of the main computational domain is shown for each isosurface. As we can see from these isosurfaces, the evolution processes of the amplitudes of perturbations for spherical and cylindrical converging RMI are basically identical. Firstly, the phase inversion phenomenon is observed as the shock wave converges from the heavy fluid into the light fluid. The amplitudes of the perturbations decrease after the shock waves first pass through the interfaces from the heavy fluids, so that the isosurfaces are smoother at $t = 0.01$ ms. Then, the reflected shock waves interact with the interfaces secondly, resulting in abundant large-scale bubble structures being generated on the interfaces (see the isosurfaces at $t = 0.02$ ms and 0.04 ms). Finally, these large-scale bubbles interact with each other and break into a large number of small-scale structures, and the turbulent mixing begins (see the isosurfaces at $t = 0.08$ ms and 0.2 ms).

The shock wave is the main driving force and energy source of RMI. Therefore, it is of great physical significance to correctly capture the trajectory of the shock wave. Figure 6 shows the wave diagram illustrating the main shock wave positions, r_s, and the outer radii of the mixing layers for spherical and cylindrical converging RMI. The shock wave positions are identified by the absolute maximum of velocity divergence, i.e. $\max(|\nabla \cdot V|)$. As shown in figure 6, before the converging shock waves pass through the interfaces for the first time, i.e. $t < 0.005$ ms, the velocities of the spherical and cylindrical converging shock waves are identical. After the shock waves are incident into light fluids from heavy fluids, the velocities of the shock waves increase obviously due to the changes of specific heat ratios, and the velocity of the spherical converging shock wave is faster than that of the cylindrical converging shock wave. The spherical transmitted shock wave arrives at the converging centre point at $t = 0.019$ ms. The cylindrical transmitted shock wave arrives at the converging centre line at $t = 0.021$ ms. Transmitted shock waves are reflected at the converging centres and transformed into reflected shock waves. After reflections, the difference of velocity difference between spherical and cylindrical reflected shock waves is further enlarged. The spherical reflected shock wave interacts with the interface at $t = 0.026$ ms, and the cylindrical reflected shock wave passes through the interface at $t = 0.03$ ms. Due to the decreases of specific heat ratios, the velocities of the reflected shock waves become slower after they are transmitted from light fluids into heavy fluids. In a word, the geometric effect (sphere or cylinder) has a great impact on the trajectory of the shock wave.

The mixing layer width of RMI is one of the most important physical quantities in practical engineering applications. Studies on the planar RMI show that the increase of the turbulent mixing layer width follows the law of $h \sim t^{\theta}$. However, different studies have given different exponents θ.

The time evolutions of the mixing layer widths for spherical and cylindrical converging RMI are shown in figure 7. The mixing layer width h are defined as

$$h = r_2 - r_1. \tag{3.1}$$

It can be seen from figure 7 that, after the shock waves interact with interfaces for the first time, the initial mixing layer widths are compressed and reduce to the minimum values. From here until $t = 0.026$ ms for the spherical mixing layer and $t = 0.03$ ms for

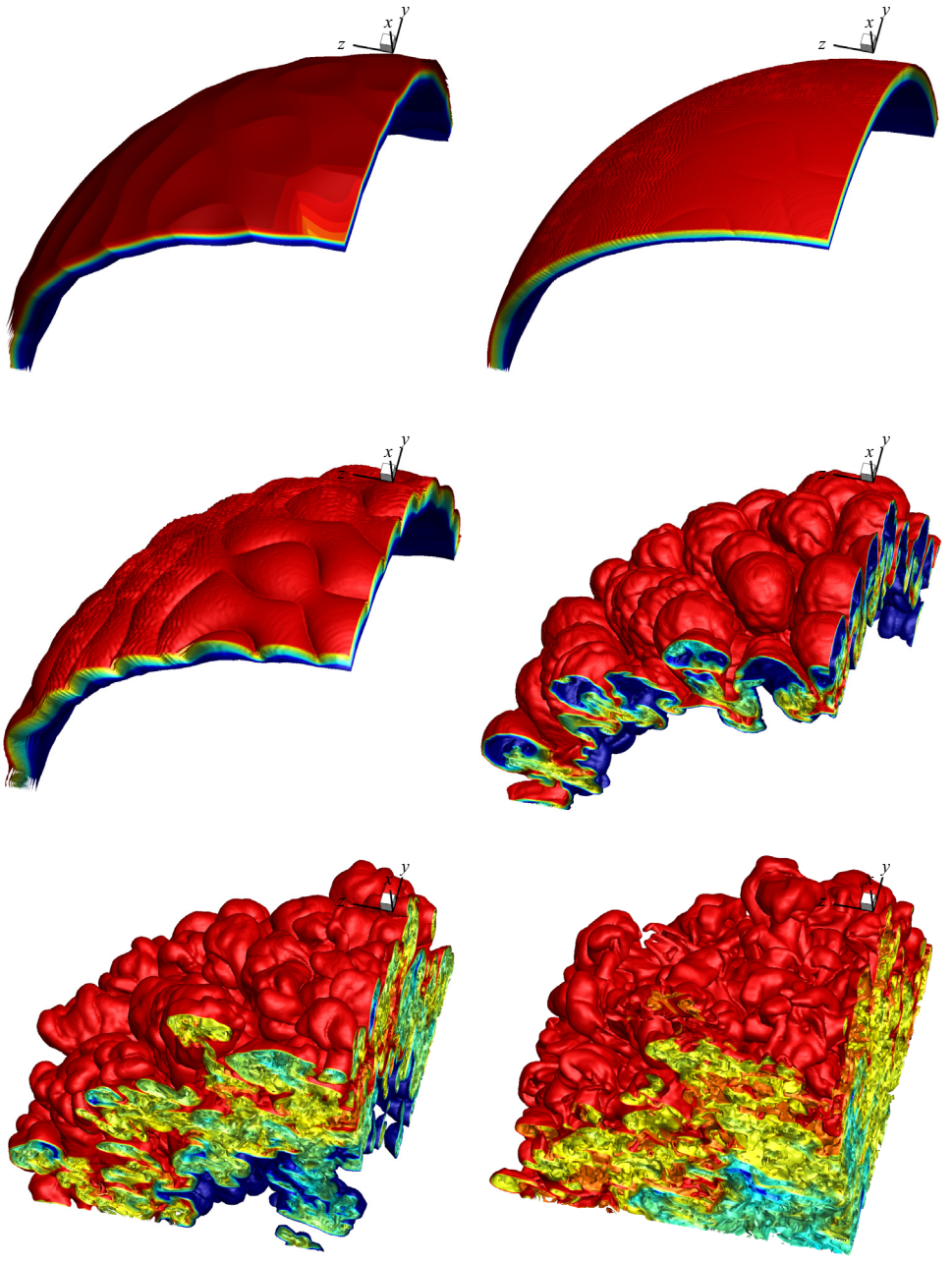

Figure 4. Isosurfaces of mass fraction of SF6 for spherical converging RMI at $t = 0$ ms, 0.01 ms, 0.02 ms, 0.04 ms, 0.08 ms and 0.2 ms. Only one eighth of the main computational domain is shown for each isosurface.

the cylindrical mixing layer, the heavy fluids accelerate the light fluids in the mixing layers, so the flow is RT stable. The RT stable effect results in a weak or even negative growth of the mixing layer width. After the reflected shock waves impact interfaces again, the light fluids accelerate the heavy fluids in the mixing layers, and the flow is RT unstable. The mixing layer widths begin to grow rapidly, first linearly, then nonlinearly and finally

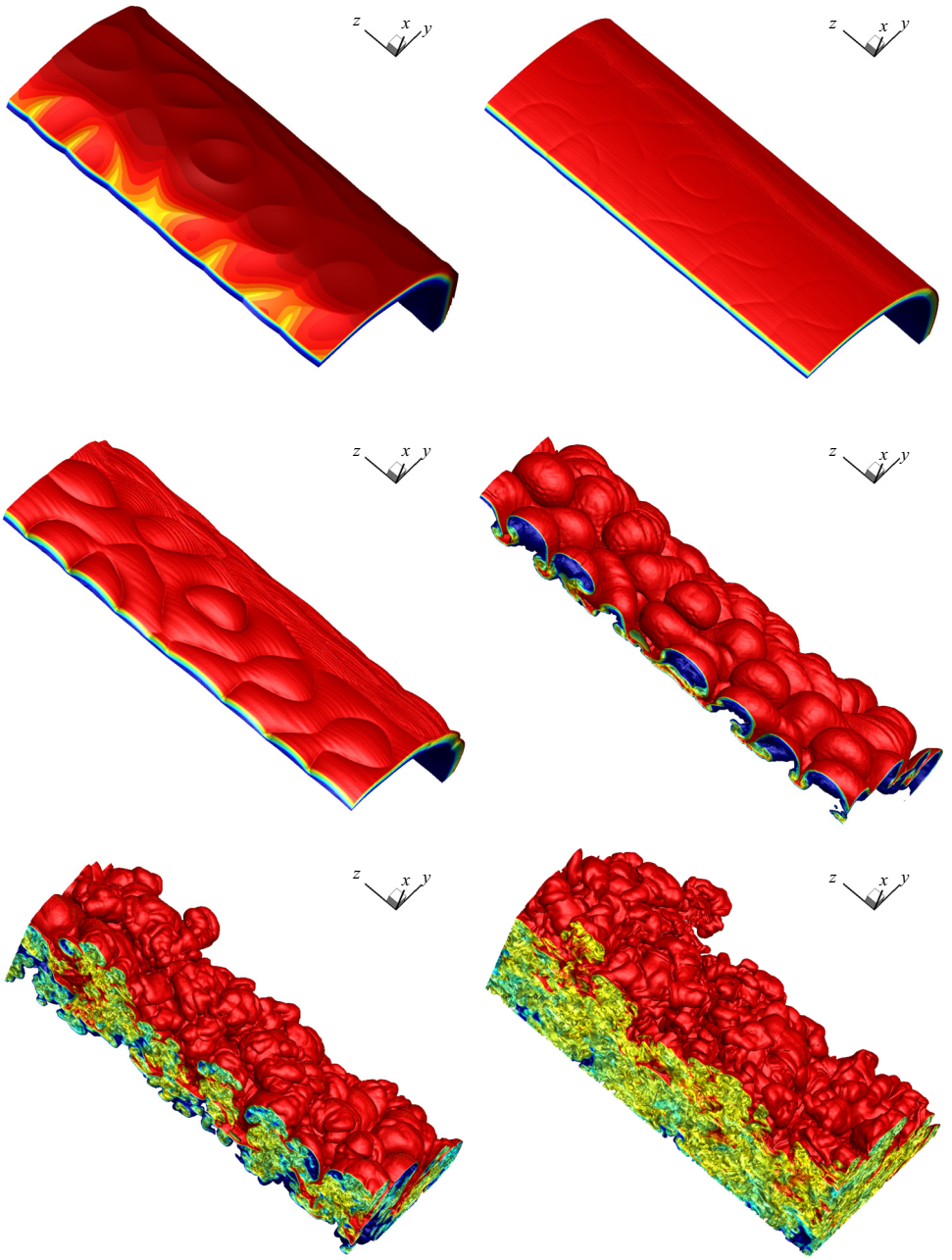

Figure 5. Isosurfaces of mass fraction of SF6 for cylindrical converging RMI at $t = 0$ ms, 0.01 ms, 0.02 ms, 0.04 ms, 0.08 ms and 0.2 ms. Only one eighth of the main computational domain is shown for each isosurface.

reach the asymptotic saturation levels. In the linear growth stage, for spherical converging RMI, the mixing layer width varies as $h \sim 0.7tU_r$. For the cylindrical converging RMI, the mixing layer width varies as $h \sim 0.58tU_r$, which indicates that the linear growth rate of the cylindrical mixing layer is approximately 17 % lower than that of the spherical mixing layer. The asymptotic values of spherical and cylindrical mixing layer widths are

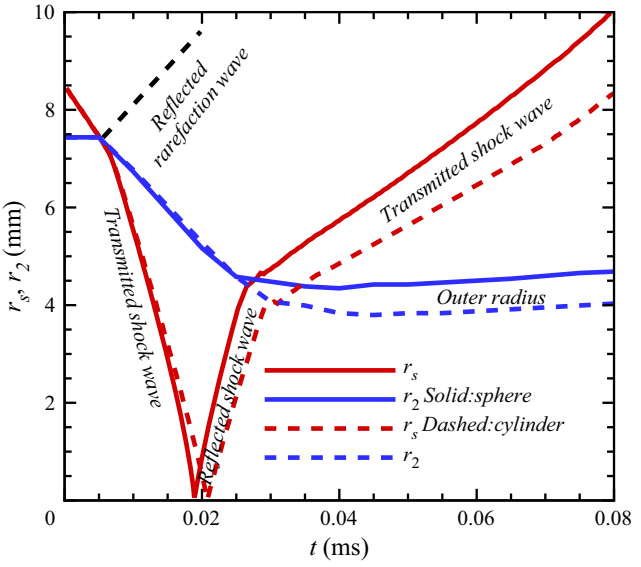

Figure 6. Wave diagram showing main shock wave positions and the outer radii of the mixing layers.

5.1 mm($0.73R_0$) and 4.6 mm($0.66R_0$), respectively. There is a difference of approximately 10 % between the asymptotic values of spherical and cylindrical mixing layer widths. On the whole, the geometric effect has a great influence on the developments of the mixing layer widths, and the width of spherical mixing layer is obviously larger than that of the cylindrical mixing layer. The main reason for this phenomenon may be that the spherical mixing layer converges toward the centre point from three directions, while the cylindrical mixing layer converges toward the centre line from only two directions, so that the BP effect of spherical converging geometric is stronger.

According to the inner and outer radii of the mixing layer, the heights of the bubble (light fluid penetrates heavy fluid) and spike (heavy fluid penetrates light fluid) can be defined as,

$$h_b = r_2 - r_{0.5}, \quad h_s = r_1 - r_{0.5}. \tag{3.2a,b}$$

Here, the $r_{0.5}$ denotes the position where the mass fractions of light and heavy fluids both are 0.5. It can be clearly seen from figure 8 that, for the cylindrical converging RMI, the bubble height always increases linearly and gently. For the spherical converging RMI, the bubble height has a rapid growth stage (approximately in the range 0.05 ms $< t <$ 0.07 ms). This is mainly because the spherical mixing layer has a geometric divergence effect outwards. However, as large-scale bubbles interfere with each other and break into small-scale structures, the mixing layer enters the turbulent mixing stage, and the spherical geometrical outward divergence effect no longer plays a dominant role. Then, the bubble height of spherical mixing layer also enters a slow linear growth stage. For spherical and cylindrical converging RMI, the spikes reach the centre at approximately 0.1 ms, and from then on the spike positions remains constant.

Figure 9 displays the time developments of mass fractions of SF6 in the mixing layers. The distribution of mass fraction can, to a certain extent, characterize the mixing degree of the two fluids, which includes not only the mixing at the molecular level, but also the mixing of pure light/heavy fluid entering into heavy/light fluid through the

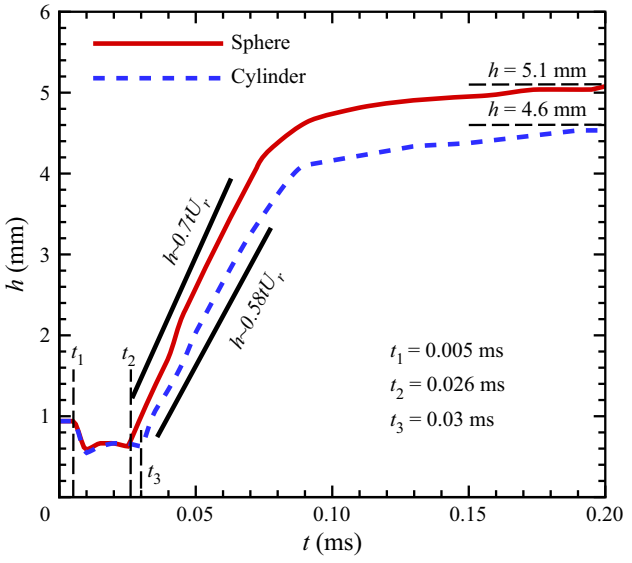

Figure 7. The width of the mixing layer vs. time. Here, t_1 is the moment when the shock waves first hit the interfaces; t_2 and t_3 are the moments when the spherical and cylindrical reflected shock waves hit the interfaces for the second time, respectively.

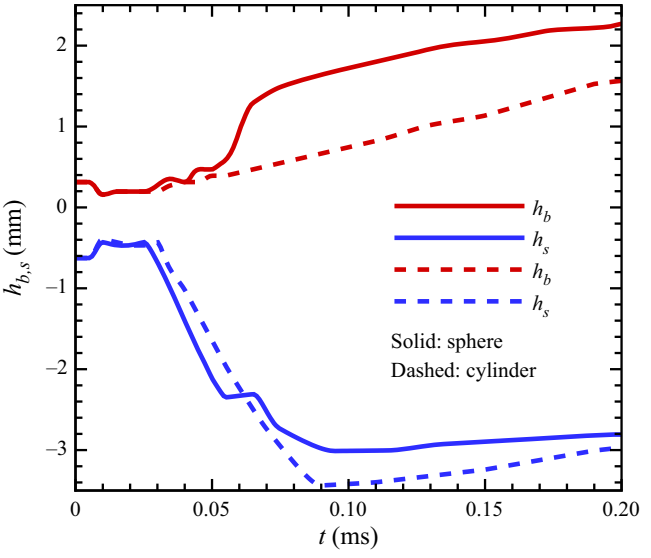

Figure 8. The heights of the bubble and spike vs. time.

bubble/spike structures and still maintaining the pure fluid state. As shown in figure 9, before the reflected shock waves pass through mixing layers, the mass fractions of SF6 in the spherical and cylindrical mixing layers are roughly the same. The main reason is that the first interactions between converging shock waves and interfaces cause the amplitudes of interfacial perturbations to decrease. Meanwhile, the bubble and spike structures are relatively small and develop slowly, and the influences of the geometric effect are insignificant. In addition, as the shock waves converge from the heavy fluids into

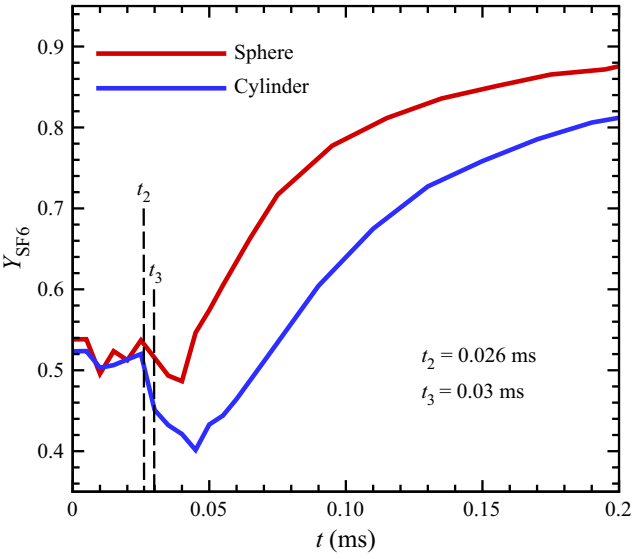

Figure 9. Mass fraction of SF6 in the mixing layer vs. time.

the light fluids, so-called phase inversion phenomena occur, that is, the amplitudes of the initial perturbations on the interfaces first decrease and then increase in reverse. In other words, the light and heavy fluids first separate from each other, and then penetrate each other, which is also the reasons that the mass fraction of SF6 fluctuates during this stage. After the second interactions between reflected shock waves and interfaces, the widths of the spherical and cylindrical mixing layers start to grow quickly and the bubble and spike structures develop rapidly so that a large amount of pure fluids are brought into the other pure fluids. During this stage, the geometric effect becomes very important, resulting in a large difference in the mass fractions of SF6 in spherical and cylindrical mixing layers, and the mass fraction of SF6 in the spherical mixing layer is significantly higher than that in the cylindrical mixing layer. This means that the spherical mixing layer brings more SF6 from the periphery into the mixing layer. For spherical and cylindrical mixing layers, the light fluid is completely mixed after approximately 0.1 ms. Thus, the mass of light fluids in the mixing layer remains constant and only the mass of heavy fluids increases. This is also why the mass fractions of SF6 are large at the end of the two numerical simulations.

For viscous flow, physical viscosity can dissipate the small-scale structures and convert kinetic energy into internal energy. The Taylor microscale is the length scale at which viscosity begins to have a significant effect on the flow. Here, the radial Taylor microscale λ is defined as,

$$\lambda^2 = \frac{\langle u_r''^2 \rangle}{\langle (\partial u''_r/\partial r)^2 \rangle}. \tag{3.3}$$

The Taylor Reynolds number Re_λ based on the Taylor microscale and Reynolds number Re_h based on the mixing layer width can be defined as, respectively,

$$Re_\lambda = \frac{u_{rms}\lambda}{\nu}, \quad Re_h = \frac{u_{rms}h}{\nu}. \tag{3.4a,b}$$

Here, $u_{rms}(=\sqrt{\langle u_r''^2\rangle})$ and $\nu(=\mu/\rho)$ are the root mean square of the radial velocity and the kinematic viscosity in the entire mixing layer, respectively. As shown in figure 10(*a*), the maximum peak values of the time evolutions of the radial Taylor microscales in the spherical and cylindrical mixing layers both are approximately 0.1 mm ($\approx 0.014R_0$). Combined with figure 7, it can be found that the radial Taylor microscales basically tend to remain unchanged after the end of the linear growth stages of the mixing layer widths. The asymptotic values of the radial Taylor microscales for spherical and cylindrical mixing layers are approximately 0.08 mm ($\approx 0.011R_0$) and 0.095 mm ($\approx 0.014R_0$) respectively. In addition, it is important to note that the radial Taylor microscale is very dependent on the mesh resolution. Figure 10(*b*) describes the time developments of the Taylor Reynolds numbers. The maximum peak value of the Taylor Reynolds number in the spherical mixing layer is approximately 2000. However, the maximum peak value of the Taylor Reynolds number in the cylindrical mixing layer is only approximately 1000, which only is half of that in the spherical mixing layer. In the late stage, the Taylor Reynolds numbers in the spherical and cylindrical mixing layers gradually decay to the same value. The time development of the Reynolds numbers based on the mixing layer width is shown in figure 10(*c*). The peak value of Re_h for the spherical mixing layer is approximately 48 000. However, it is only approximately 31 000 for the cylindrical mixing layer.

The helicity h_t is also a noteworthy quantity, and is defined as,

$$h_t = u_i\omega_i, \tag{3.5}$$

where ω_i denotes the velocity curl. The helicity is a quadratic invariant in addition to the kinetic energy of the three-dimensional NS equations in the inviscid limit. Yu *et al.* (2013) proposed a LES model by considering the inertial range balance of subgrid-scale helicity dissipation in physical and spectral spaces and the joint cascade of energy and helicity. Therefore, the studies on the evolution mechanisms of helicity in the turbulent mixing layer induced by RMI are helpful to establish a new model or improve the existing model for the turbulent mixing problem. The time developments of helicity in the mixing layers are displayed in figure 11. After the reflected shock waves hit the interfaces for the second time, the helicity begins to increase rapidly. On the whole, compared with the cylindrical mixing layer, the spherical mixing layer has higher helicity. The peak of helicity appears at approximately $t = 0.055$ ms. The radial distribution of helicity at $t = 0.055$ ms is shown in figure 12(*a*). It can be found that, at this moment, the helicity in the spherical and cylindrical mixing layers has a regular and similar chirality. Due to the effect of viscous dissipation, the average helicities both tend to be zero at the later stage of spherical and cylindrical mixing layers. The radial distribution of helicity at $t = 0.2$ ms is shown in figure 12(*b*). At this moment, the helicity in the mixing layer has no regular chirality and shows the characteristic of fluctuating up and down around zero.

The time evolutions of the root mean square of the velocities and turbulent kinetic energy (TKE) in the mixing layers are shown in figure 13. Here, the turbulent kinetic energy is defined as,

$$TKE = \tfrac{1}{2}\langle\rho u_i'' u_i''\rangle/\langle\rho\rangle. \tag{3.6}$$

As shown in figure 13, for both the spherical mixing layer and the cylindrical mixing layer, the time development trend of TKE is very similar to that of the root mean square of the velocities. The difference is that the root mean square of the velocities and the TKE in the spherical mixing layer exhibit a single peak characteristic. However, they show a three-peak characteristic in the cylindrical mixing layer, although the third peak may be

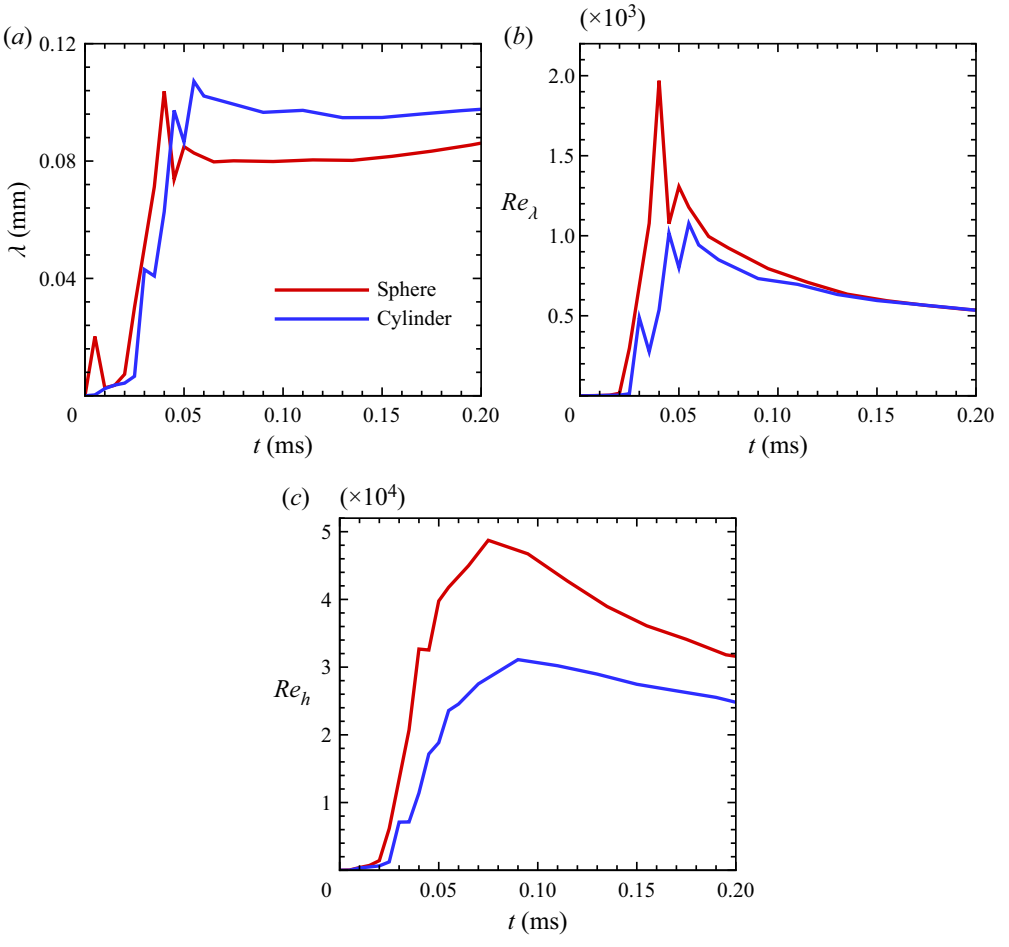

Figure 10. Radial Taylor microscale (*a*), Taylor Reynolds number (*b*) and Reynolds number based on mixing layer width (*c*) vs. time.

less obvious. The reason for this difference may be that different geometries have different reflection or transmission effects on shock waves. At the later stage, the root mean square of the velocities in the cylindrical mixing layer are at least approximately 50 % larger than that in the spherical mixing layer, which indicates that the turbulent intensity in the cylindrical mixing layer is higher. In terms of TKE, after $t > 0.1$ ms, at this time when the spherical and cylindrical mixing layer widths begin to reach asymptotic saturation, the TKEs have a power-law decay with time, i.e. $TKE \sim t^{-n}$. Groom & Thornber (2021) find that the decay rate n of TKE is 1.51–2.20 in planar RMI, and the decay rate decreases with increasing initial Reynolds number. In the present numerical simulations, the decay exponents of the TKE in spherical and cylindrical mixing layers both are $n = 2.20$. This indicates that the turbulent mixing effect is more dominant than the geometric effect in the turbulent mixing stage.

As mentioned above, the RMI is mainly caused by the baroclinic vorticity. Therefore, the analysis of the physical quantities related to the vortex dynamics can deepen our understanding of the intrinsic mechanism of RMI. In our previous paper (Fu *et al.* 2020),

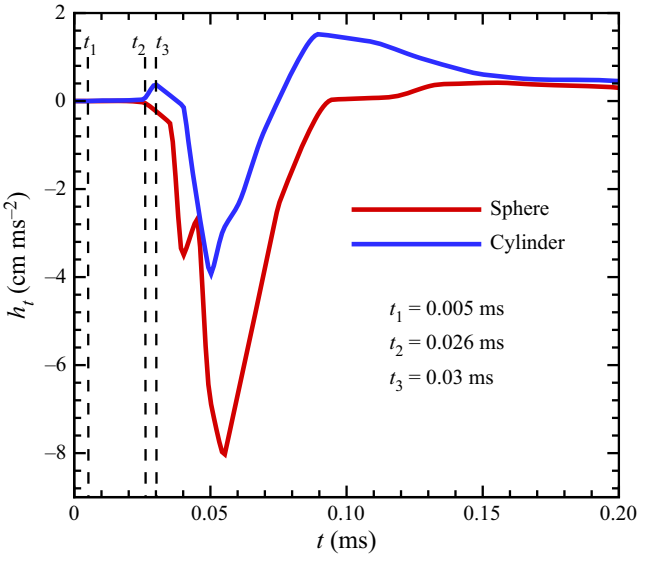

Figure 11. Helicity in the mixing layer vs. time.

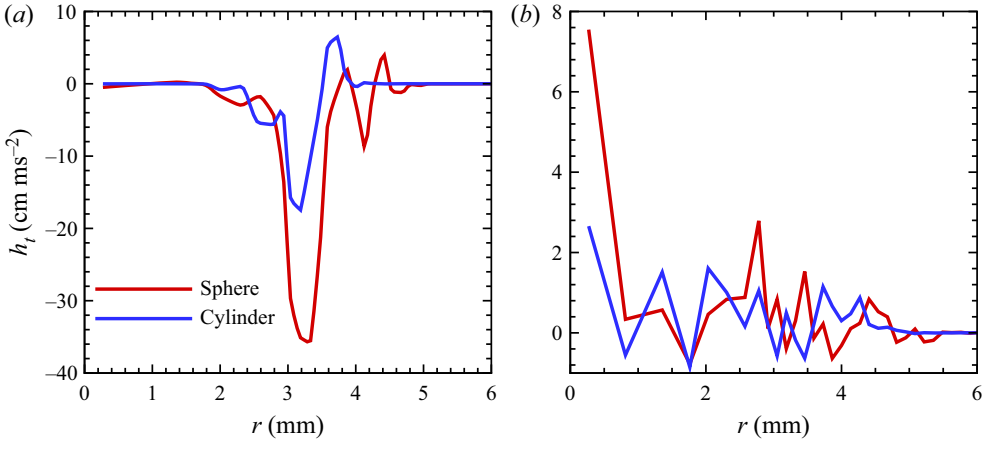

Figure 12. Radial distribution of helicity at $t = 0.055$ ms (a) and $t = 0.2$ ms (b).

the enstrophy transport equation has been analysed in detail. The enstrophy is defined as,

$$\Omega = \tfrac{1}{2}\omega_i\omega_i. \tag{3.7}$$

Figure 14 shows the time evolutions of the enstrophy in the spherical and cylindrical mixing layers. From figure 14(a,b), it can be found that, for both spherical and cylindrical converging RMI, refining the mesh greatly increases the enstrophy, which is similar to the numerical results of Hahn *et al.* (2011). In addition, we also find that the quantities that do not include the partial derivatives of the velocities have reached mesh convergence, while the quantities that include the partial derivatives of the velocities, such as the dissipation rate, enstrophy and Taylor scale, have not reached mesh convergence. This is a consequence of using the ILES approach which resolves more and more of the fine-scale structure as the mesh is refined. The peak value of enstrophy in the spherical mixing layer

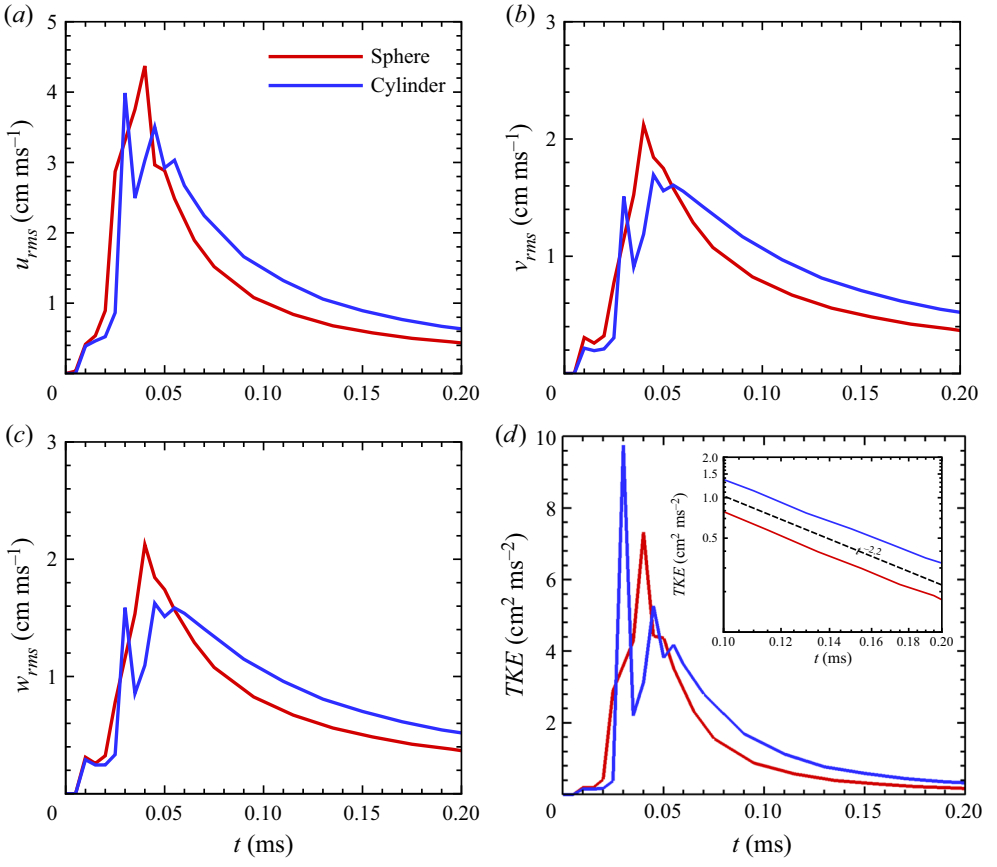

Figure 13. Root mean square of velocities (*a–c*) and turbulent kinetic energy (*d*) in the mixing layer vs. time. For spherical converging RMI, u is the radial velocity, v is velocity in the $\varphi(0 \leq \varphi \leq 2\pi)$ direction, w is the velocity in the $\theta(0 \leq \varphi \leq \pi)$ direction. For cylindrical converging RMI, u is the radial velocity, v is the velocity in the $\varphi(0 \leq \varphi \leq 2\pi)$ direction, w is the velocity in the z direction.

is much larger than that in the cylindrical mixing layer. Combined with figure 7, it can be found that the time interval corresponding to the linear growth stage of mixing layers is approximately 0.03 ms $< t <$ 0.08 ms, which is exactly consistent with the peak interval of enstrophy. And outside of this time interval, the enstrophy tends to be zero. Therefore, it can be concluded that the developments of enstrophy are closely related to the increases of the mixing layer widths, and larger enstrophy is more conducive to the growth of the mixing layer widths. When the spherical and cylindrical mixing layer widths begin to reach asymptotic saturation (approximately $t > 0.1$ ms), the enstrophy has a power-law decay with time, i.e. $\Omega \sim t^{-a}$. In the spherical mixing layer, the decay exponents of enstrophy is $a = 2.58$. In the cylindrical mixing layer, the decay exponents of enstrophy is $a = 2.42$. The geometric effect has little effect on the decay exponent of enstrophy.

The probability density functions (PDF) of the mass fractions of SF6 in the spherical and cylindrical mixing layers at $t = 0.2$ ms are displayed in figure 15. It can be found that the PDF of the mass fractions of SF6 in spherical and cylindrical mixing layers have bimodal characteristics. The first peak value of the PDF appears at the position of $Y_{SF6} = 0.89$ in the spherical mixing layer, and at the position of $Y_{SF6} = 0.8$ in the cylindrical mixing layer.

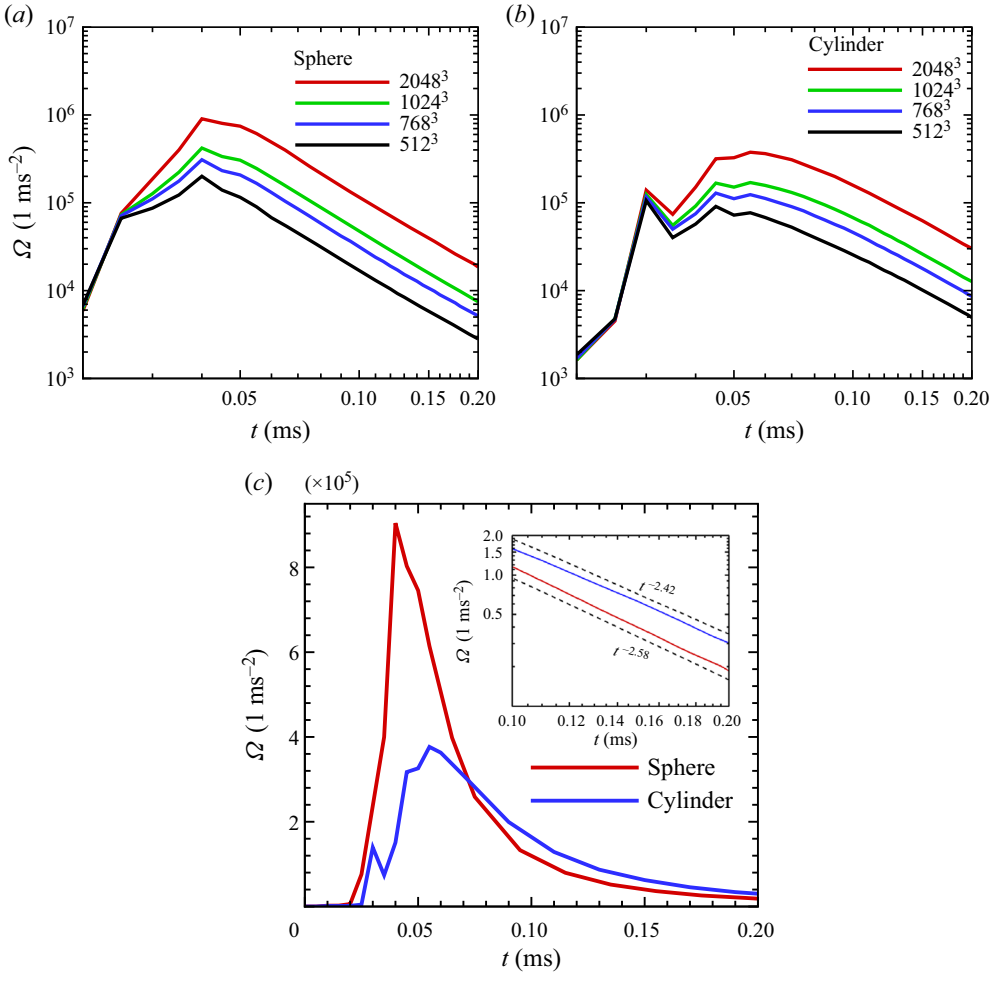

Figure 14. Enstrophy in the mixing layer vs. time.

The second peak values of the PDF appear at the positions of $Y_{SF6} = 1$, which indicates that there is still a large amount of pure SF6 in the mixing layers. In the range of low mass fraction, the PDF in the cylindrical mixing layer is larger, and the left tail is flatter, which shows that the mixing degree between light and heavy fluids in the spherical mixing layer is greater than that in the cylindrical mixing layer.

Figure 16 describes the time developments of the skewness and kurtosis factors in the spherical and cylindrical mixing layers. The skewness and kurtosis factors can be used to describe the degree of deviation of the radial fluctuation velocity from the Gaussian distribution due to the existence of turbulent intermittency. If a random variable of zero mean is Gaussian, then its skewness factor S would be equal to 0 and kurtosis factor K would be equal to 3. In addition, the skewness factor can also characterize the rate at which the enstrophy increase by vortex stretching, and the equation is $s = (135/98)^{1/2}\langle\omega_i\omega_j(\partial u_i/\partial x_j)\rangle/\Omega^{3/2}$ (Lesieur 1997). Figure 16 shows that at the later turbulent mixing stage, both the skewness and kurtosis factors of the radial fluctuation velocity in the cylindrical mixing layer are larger, indicating stronger turbulent intermittency.

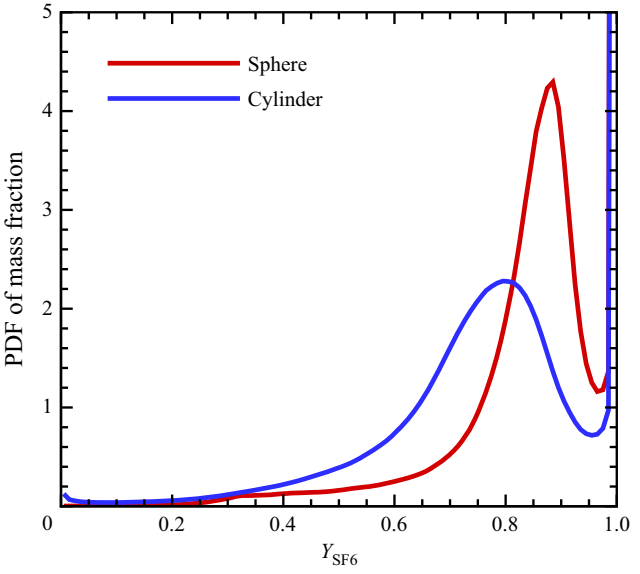

Figure 15. Probability density function of the mass fraction of SF6 in the mixing layer at $t = 0.2$ ms.

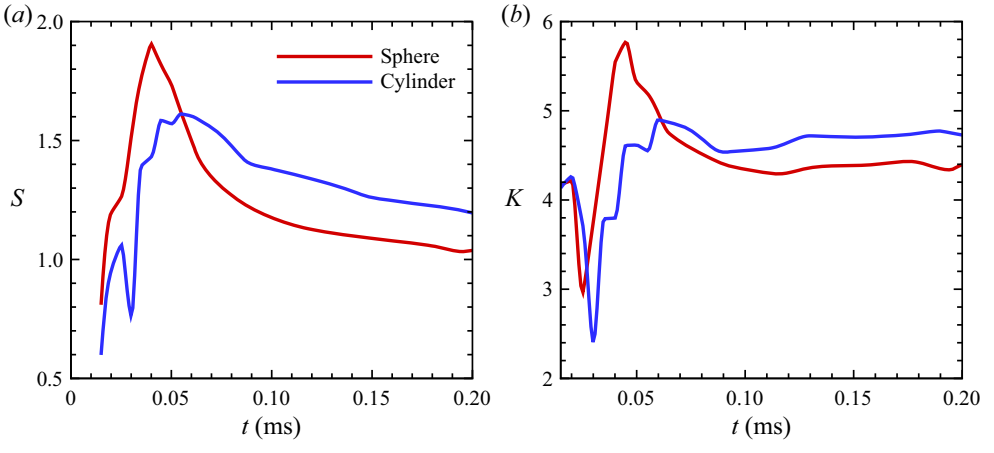

Figure 16. Skewness (*a*) and kurtosis factors (*b*) in the mixing layer vs. time.

The mixing layer width and mass fraction distribution can, to some extent, characterize the mixing degree of different fluids, but, as mentioned above, these two quantities cannot distinguish whether the mixing is true molecular-level mixing. There are many parameters that have been proposed to measure the molecular mixing degree. Zhou *et al.* (2016) compared in detail the asymptotic behaviour of different mixing parameters in plane RTI and RMI with different density ratios. In this paper, the molecular mixing fraction θ defined by Youngs (1991, 1994) is used to measure the molecular mixing degree

$$\theta = \frac{\int X_1 X_2 \, \mathrm{d}V}{\int \langle X_1 \rangle \langle X_2 \rangle \, \mathrm{d}V}. \tag{3.8}$$

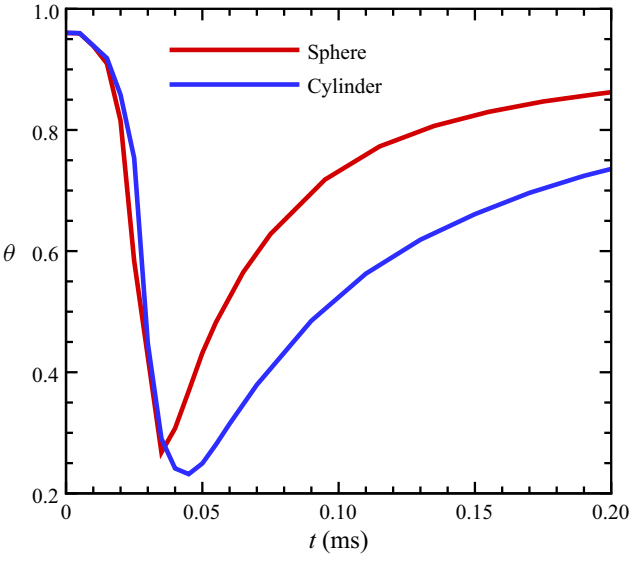

Figure 17. Molecular mixing fraction vs. time.

Here, $\theta = 1$ denotes perfect mixing and $\theta = 0$ denotes complete separation; X_k denotes the volume fraction of species k. The time developments of the molecular mixing fractions of the spherical and cylindrical mixing layers are shown in figure 17. The molecular mixing fractions of spherical and cylindrical mixing layers first decrease monotonically and then increase monotonically. This is because, at the early stage, the mixing layer is mainly composed of pure fluids that penetrate each other. The molecular mixing fraction decreases with the increase of the bubble and spike structures. After the reflected shock, the pure fluid begins to break up into small structures and molecular mixing causes the molecular mixing fraction to increase again. At the later stage, the increases of molecular mixing fractions slow down and begin to reach the asymptotic values. At the growth stage, the molecular mixing fraction in the spherical mixing layer is always larger. In other words, the fluid in spherical mixing layer is more fully mixed. In addition, comparing figure 17 with figure 14, it can be found that the time interval corresponding to the fastest growth rates of molecular mixing fractions is basically consistent with the peak interval of enstrophy and linear growth interval of the mixing layer width. This is mainly because the magnitudes of enstrophy can represent the strength of vorticity, and the rotational motions of the vortex can accelerate the mixing between light and heavy fluids.

The efficiency Atwood number can be defined as,

$$A_e = \frac{\rho_{rms}}{\langle \rho \rangle}. \tag{3.9}$$

The efficiency Atwood number is a quantity related to the turbulent mixing and mixing layer width growth. As A_e decreases, the entrainment, which is responsible for bringing the large pockets of irrotational fluid into the turbulent flow region, is weakened gradually and the turbulent mixing is strengthened gradually. Conversely, when A_e increases, pure fluids come into the turbulent flow region faster than they are mixed. Cook, Cabot & Miller (2004) believe that, at the stage of mixing transition, the turbulent mixing rate overtakes the entrainment rate so that the growth rate of the mixing layer width is reduced. As shown in figure 18, the time evolution trends of the efficiency Atwood numbers in the spherical

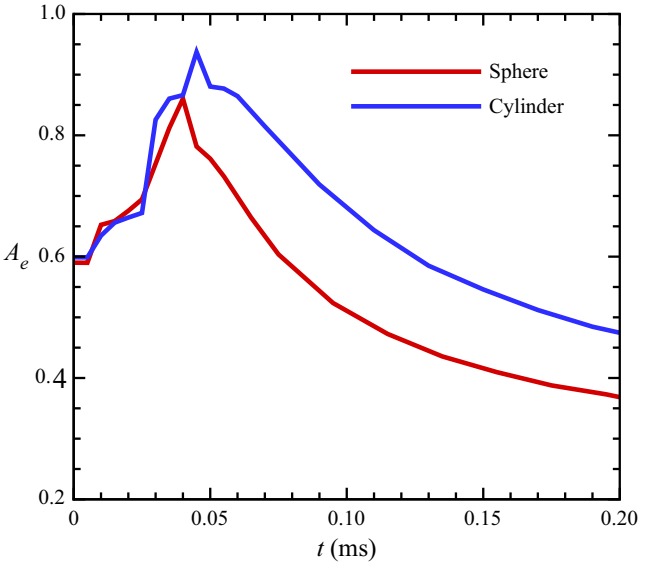

Figure 18. Efficiency Atwood number in the mixing layer vs. time.

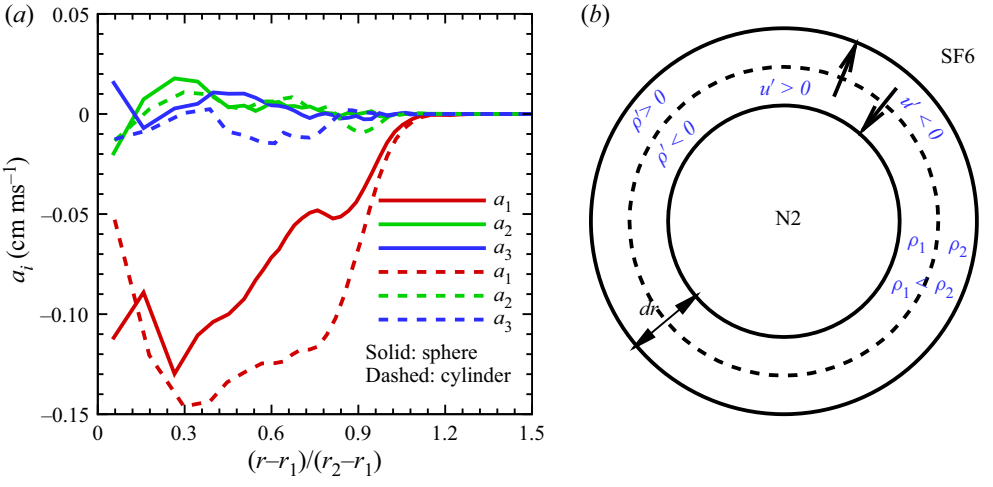

Figure 19. (*a*) Radial distribution of turbulent mass-flux velocity at $t = 0.2$ ms. (*b*) schematic of radial turbulent mass-flux velocity.

and cylindrical mixing layers are the inverse of the molecular mixing fractions. This reason is that the efficiency Atwood number increases monotonically, indicating that the turbulent mixing rate is weakening compared with the entrainment rate, so the molecular mixing fraction decreases monotonically. Conversely, the efficiency Atwood number decreases monotonically, indicating that the turbulent mixing is being intensified, so the molecular mixing fraction increases monotonically. At the later stage, the efficiency Atwood number in the spherical mixing layer is always smaller, indicating that the turbulent mixing rate is faster in the spherical mixing layer.

The turbulent mass-flux velocity $a_i = -\langle u'' \rangle$ is also an important source term related to turbulent mixing. For the three-equation Reynolds-averaged Navier–Stokes model,

i.e. $k{-}L{-}a$ mode (Morgan & Wickett 2015), the turbulent mass-flux velocity as a prefactor appears in the energy equation, TKE equation and turbulent mass-flux velocity equation. Therefore, the study of the turbulent mass-flux velocity is beneficial to improve the turbulent mixing model. Mohaghar *et al.* (2017) and Reese *et al.* (2018) use the density-weighted turbulent mass-flux velocity $a_i = \langle \rho' u_i' \rangle / \langle \rho \rangle$ in their papers instead of $-\langle u'' \rangle$. However, it can be proved that these two are equal, i.e.

$$a_i = -\langle u'' \rangle = \left\langle \frac{\langle \rho u \rangle}{\langle \rho \rangle} - \frac{\langle \rho \rangle u}{\langle \rho \rangle} \right\rangle = \left\langle \frac{\langle \rho \rangle \langle u \rangle + \langle \rho' u' \rangle - \langle \rho \rangle \langle u \rangle - \langle \rho \rangle u'}{\langle \rho \rangle} \right\rangle = \frac{\langle \rho' u' \rangle}{\langle \rho \rangle}. \quad (3.10)$$

The radial distributions of turbulent mass-flux velocities at $t = 0.2$ ms for spherical and cylindrical mixing layers are shown in figure 19(*a*). The radial distance is normalized by the inner and outer radii of mixing layer. First, it can be found that the turbulent masses are transported mainly in the radial directions. In addition, the radial turbulent mass-flux velocities a_1 in the mixing layers are all negative. However, a_1 being predominantly negative does not indicate net negative fluctuation, or the transport of turbulence and mass inwards. It indicates that, in a spherical or cylindrical averaging shell (as shown in figure 19*b*), the negative mass fluctuations are paired with positive radial velocity fluctuations, and positive mass fluctuations are correlated with negative radial velocity fluctuations. In other words, the light fluids are being transported from the centre outward, and the heavy fluids are being transported from the periphery inward. This leads to mutual penetration and turbulent mixing between the two fluids. The larger the turbulent mass-flux velocity is, the more intense the turbulent mass exchange is. At the later stage, because the species in the spherical mixing layer have been mixed more fully, the turbulent mass-flux velocity is generally smaller than that in the cylindrical mixing layer. The values of a_2 and a_3 both are close to zero, which means that the mass and velocity fluctuations are uncorrelated, without a preferential direction of transport over the whole radial spherical or cylindrical shell.

The density self-correlation b can also be used to measure the fluid mixing and is defined as,

$$b = -\left\langle \rho' \left(\frac{1}{\rho} \right)' \right\rangle. \quad (3.11)$$

Here, $b = 0$ indicates that the fluid is perfect mixed fluid or pure fluid. The density self-correlation as a prefactor appears in the production term of the turbulent mass-flux velocity equation in the $k - L - a$ model and is closed by a algebraic equation, i.e.

$$b = \bar{\rho} \left(\frac{\sum_k \frac{X_k}{\rho_k + c\bar{\rho}}}{\sum_k \frac{X_k \rho_k}{\rho_k + c\bar{\rho}}} \right) - 1. \quad (3.12)$$

Here, c is an undetermined model constant and is set as zero through similarity analysis. The radial distributions of the density self-correlations calculated by using (3.11) and (3.12) for spherical and cylindrical mixing layers at $t = 0.2$ ms are shown in figure 20. For convenience of viewing, the results of (3.12) are multiplied by the corresponding coefficients to ensure that the peak values of the density self-correlations are equal. In terms of the results of (3.11), outside the mixing layers, because the fluids are pure heavy fluids, the density self-correlations are both zero for spherical and cylindrical mixing layers. In the mixing layers, the density self-correlation of the spherical mixing layer

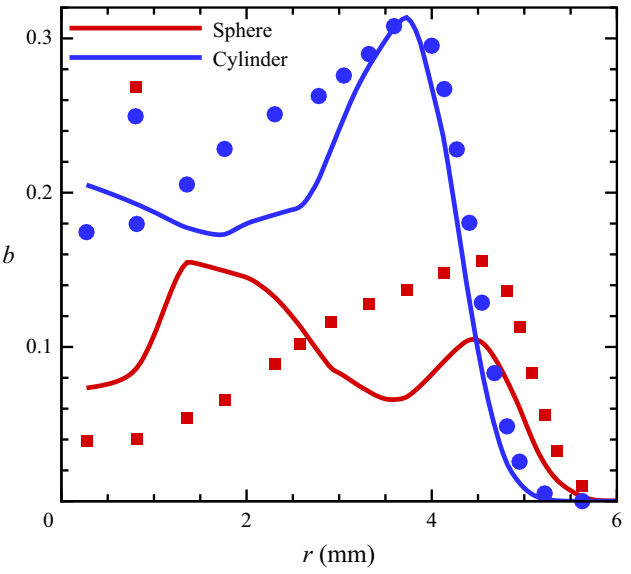

Figure 20. Radial distribution of density self-correlation at $t = 0.2$ ms. Lines are the results of (3.11); squares are the result of (3.12) with a scaling factor of 0.04 in spherical mixing; circles are the result of (3.12) with a scaling factor of 0.096 in cylindrical mixing.

is generally lower than that of the cylindrical mixing layer, which again indicates that there are more unmixed pure fluid bubbles in the cylindrical mixing layer. Comparing the results of (3.11) with (3.12) in figure 20, it can be found that the density self-correlations calculated using the algebraic equation of the k–L–a model are different in magnitude. In addition, the shapes of the radial distribution of the real results and algebraic equation results are also very different, especially for the spherical converging geometry. The main reason for this phenomenon may be that the model constant c in the k–L–a model is obtained by self-similarity analysis of one-dimensional RTI and RMI in the low Atwood number limit, and the influence of the geometric effect is also not considered. Therefore, it is necessary to improve this algebraic equation.

The Reynolds stresses are one of the most important unclosed terms in Reynolds-averaged Navier–Stokes model, which are defined as,

$$R_{ij} = \langle \rho u_i'' u_j'' \rangle. \tag{3.13}$$

Figure 21(a) describes the radial distributions of Reynolds stresses in spherical and cylindrical mixing layers at $t = 0.2$ ms. Compared with the Reynolds normal stresses (R_{11}, R_{22}, R_{33}), the Reynolds shear stresses (R_{12}, R_{13}, R_{23}) are negligible, which indicates that the shear effects in the mixing layers are very small and the turbulent production is of baroclinic type. According to the Reynolds stresses, the Reynolds stress anisotropy tensor can be defined as,

$$b_{ij} = \frac{\langle \rho u''_i u''_j \rangle}{\langle \rho u''_k u''_k \rangle} - \frac{1}{3}\delta_{ij}. \tag{3.14}$$

The value of b_{ij} is between $-1/3$ and $2/3$. If $b_{ij} = -1/3$, that means there is no TKE distributed in this direction, and if $b_{ij} = 2/3$, that means that all the TKE is occupied in this direction. The time developments of the Reynolds stress anisotropy tensors in the

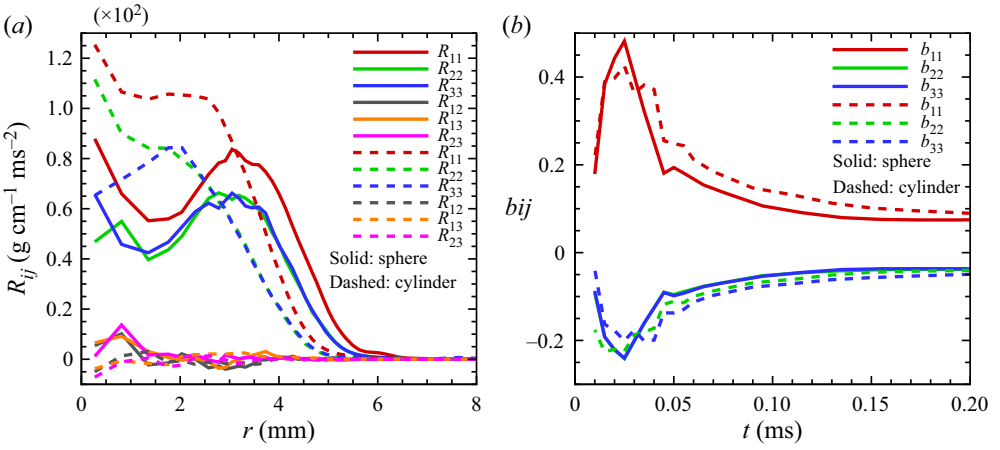

Figure 21. (*a*) Radial distribution of Reynolds stress at $t = 0.2$ ms. (*b*) Anisotropy of Reynolds stress in the mixing layer vs. time.

spherical and cylindrical mixing layers are displayed in figure 21(*b*). When the reflected shock waves pass through the interfaces for the second time, the Reynolds stress anisotropy in spherical and cylindrical mixing layers reaches its peak value. The peak values are 0.48 and 0.42 for the spherical and cylindrical mixing layers, respectively. This means that approximately 81 % of TKE is in the radial direction for the spherical mixing layer, and approximately 75 % of TKE is in the radial direction for the cylindrical mixing layer. Then, with the increase of time, the anisotropy decreases monotonically, indicating that the flows in the mixing layers are developing toward isotropy. Finally, b_{11} in the spherical mixing layer tends to 0.07, that is, approximately 40 % of TKE is distributed in the radial direction. The value of b_{11} in the cylindrical mixing layer tends to 0.09, that is, approximately 42 % of TKE is distributed in the radial direction. The spherical mixing layer is more isotropic.

Next, the method of conditional statistics will be applied in the mixing layers to study the influence of the geometric effect under given conditions. Here, conditional statistics means that, at a certain moment, within a certain space range, the data on the grid points satisfying the given condition are recombined into a new data set, and then statistical analysis is carried out on this new data set. The mass fraction is an extremely important physical quantity in the turbulent mixing induced by the interfacial instability. Therefore, in the present paper, the mass fraction of SF6 is selected as the condition to perform conditional statistics.

Figure 22 shows the conditional mean of the radial velocity in mass fraction space in the spherical and cylindrical mixing layers at $t = 0.2$ ms. It can be seen from figure 22 that the radial velocities are obviously dependent on the mass fractions. For the spherical mixing layer, when $Y_{SF6} < 0.89$, the conditional mean of the radial velocity is greater than zero. When $Y_{SF6} > 0.89$, the conditional mean of the radial velocity is smaller than zero. For the cylindrical mixing layer, when $Y_{SF6} < 0.82$, the conditional mean of the radial velocity is greater than zero. When $Y_{SF6} > 0.82$, the conditional mean of the radial velocity is smaller than zero. Combined with figure 15, it can be found that values of 0.89 and 0.82 roughly correspond to the peak values of the PDF of the mass fraction of SF6 in spherical and cylindrical mixing layers. This is mainly because the mixing degree between heavy and light fluids tends to the peak position of the PDF. Therefore, a fluid element that is less

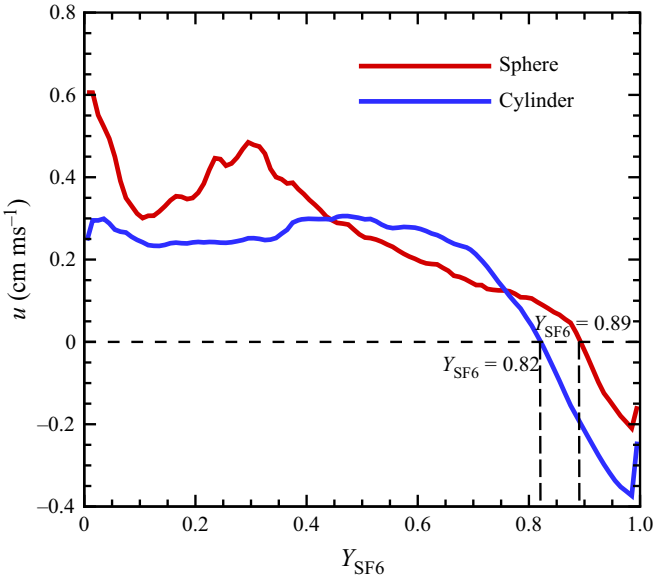

Figure 22. Conditional mean of the radial velocity in mass fraction space in the mixing layer at $t = 0.2$ ms.

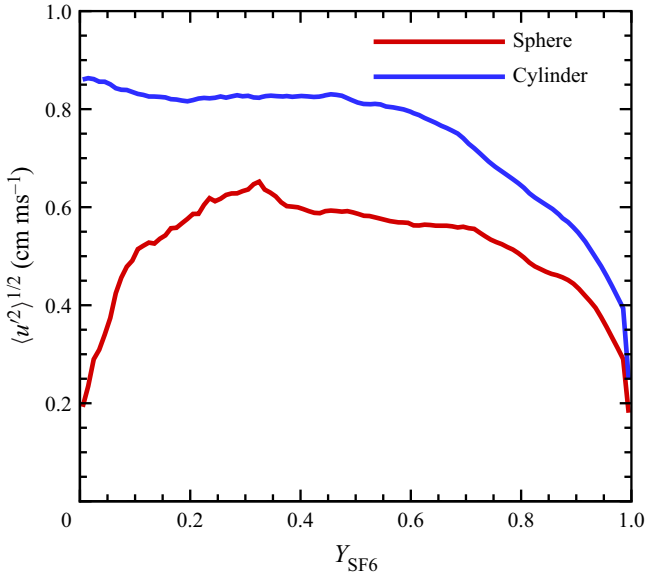

Figure 23. Conditional root mean square of the radial velocity in mass fraction space in the mixing layer at $t = 0.2$ ms.

mixed than the peak position of PDF moves outward and mixes with the SF6 fluid. A fluid element with a mixing degree greater than the peak position of PDF moves inward and mixes with the N2 fluid. Figure 23 shows the conditional root mean square of the radial velocity in mass fraction space in the spherical and cylindrical mixing layers at $t = 0.2$ ms. Obviously, in the whole mass fraction space, the conditional root mean square of the radial

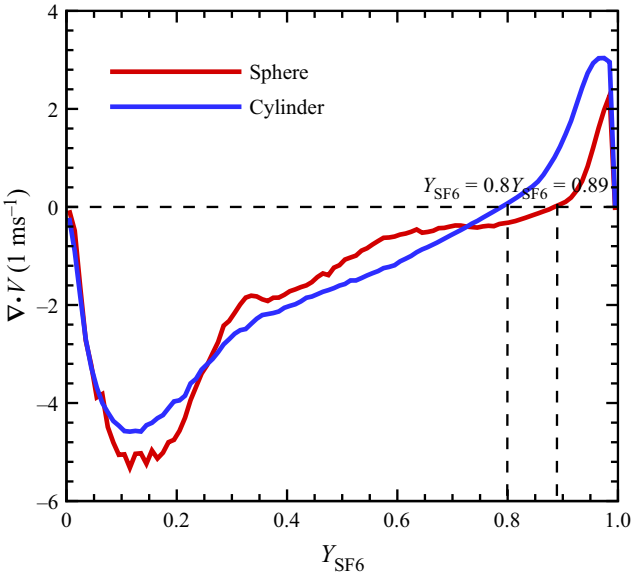

Figure 24. Conditional mean of the velocity divergence in mass fraction space in the mixing layer at $t = 0.2$ ms.

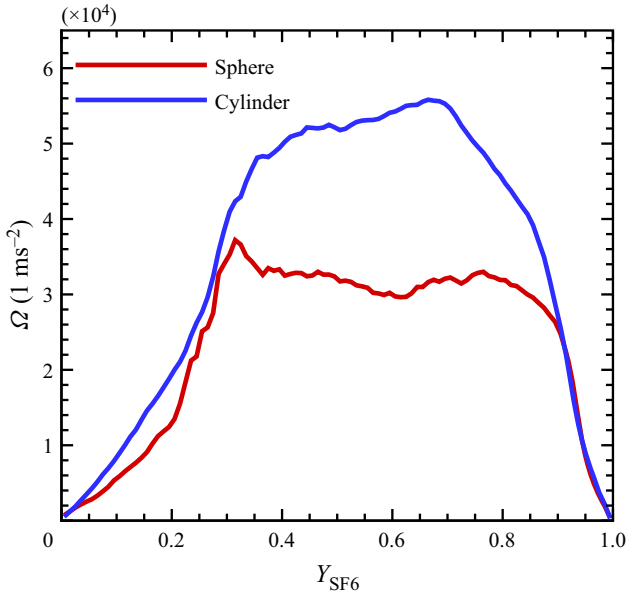

Figure 25. Conditional mean of enstrophy in mass fraction space in the mixing layer at $t = 0.2$ ms.

velocity in the cylindrical mixing layer is always larger. Therefore, it can be concluded that in the mass fraction space, the turbulent intensity is stronger in the cylindrical mixing layer.

Figure 24 shows the conditional mean of the velocity divergence in mass fraction space in the spherical and cylindrical mixing layers at $t = 0.2$ ms. The velocity divergence can be used to measure the compression and expansion effects of the fluids. If the velocity divergences are greater than zero, the fluids are expanding. Conversely, if the velocity

divergences are smaller than zero, the fluids are being compressed. We see from figure 24 that the velocity divergence is also dependent on the mass fraction. In addition, it can be found that a fluid element with a mixing degree smaller than the peak position of the PDF of the mass fraction of SF6 is compressed, and a fluid element with a mixing degree greater than the peak position of the PDF of the mass fraction of SF6 is expanding.

Figure 25 shows the conditional mean of enstrophy in mass fraction space in the spherical and cylindrical mixing layers at $t = 0.2$ ms. The enstrophy has a significant dependence on the mass fractions, and the geometric effect has a great influence on the conditional mean of enstrophy.

4. Conclusions

In this paper, comprehensive analysis is conducted for the high resolution ILES data of spherical and cylindrical converging RMI with a grid size of 2048^3. The numerical results show that,

(i) The linear growth rate of spherical mixing layer is faster than that of cylindrical mixing layer. The degree of mixing in the spherical mixing layer is greater. The turbulence in the cylindrical mixing layer is more intermittent.

(ii) Because of the geometric divergence effect outward, the bubble height has a rapid growth stage in the spherical mixing layer.

(iii) At the early stage, the helicity in the spherical and cylindrical mixing layers has a regular and similar chirality. Compared with the Reynolds normal stresses, the Reynolds shear stresses in the spherical and cylindrical mixing layers are negligible. There is strong anisotropy in the mixing layers at the early stage, but the mixing layers tend to become gradually isotropic as the developments of time. At the later stage, the TKE and enstrophy have a power-law decay with time, and the geometric effect has little effect on the decay exponent.

(iv) The conditional statistics analysis shows that the radial velocities, root mean square of the radial velocity, velocity divergence and enstrophy in the spherical and cylindrical mixing layers are obviously dependent on the mass fractions. In the mass fraction space, the turbulent intensity is stronger in the cylindrical mixing layer.

Funding. This work was supported by the National Key Research and Development Program of China (Grant Nos 2019YFA0405300, 2016YFA0401200), NSFC Projects (Grant Nos 91852203, 12072349.), the Science Challenge Project (Grant No. TZ2016001) and National Numerical Wind Tunnel Project. The authors thank the National Supercomputer Center in Tianjin (NSCC-TJ) and the National Supercomputer Center in Guangzhou (NSCC-GZ) for providing computer time.

Declaration of interests. The authors report no conflict of interest.

Author ORCIDs.
Yaowei Fu https://orcid.org/0000-0001-9261-252X;
Changping Yu https://orcid.org/0000-0002-2126-1344.

Appendix A.

In this paper, we use the polynomial fit of the logarithm of the viscosity and thermal conductivity coefficients versus the logarithm of the temperature to obtain the transport properties of species k. The coefficients of the polynomial fit can be found in tables 2 and 3.

Species	$b_{1,k}$	$b_{2,k}$	$b_{3,k}$	$b_{4,k}$
N2	$-1.554\text{E}+01$	$1.934E+00$	$-1.674E-01$	$7.228E-03$
SF6	$-1.058\text{E}+01$	$-1.114E+00$	$3.999E-01$	$-2.618E-02$

Table 2. The coefficients of polynomial fit for the viscosity of species k. The unit of the viscosity coefficient computed by using (2.7) is g (cm s)$^{-1}$.

Species	$c_{1,k}$	$c_{2,k}$	$c_{3,k}$	$c_{4,k}$
N2	$7.599E+00$	$-1.180E+00$	$3.030E-01$	$-1.539E-02$
SF6	$-8.058E+01$	$3.758E+01$	$-5.471E+00$	$2.689E-01$

Table 3. The coefficients of polynomial fit for the thermal conductivity of species k. The unit of the thermal conductivity coefficient computed by using (2.8) is erg (cm s K)$^{-1}$.

References

Bell, G.I. 1951 Taylor instability on cylinders and spheres in the small amplitude approximation. *Report* LA-1321. Los Alamos Scientific Laboratory.

Biamino, L., Jourdan, G., Mariani, C., Houas, L., Vandenboomgaerde, M. & Souffland, D. 2015 On the possibility of studying the converging Richtmyer–Meshkov instability in a conventional shock tube. *Exp. Fluids* **56**, 26.

Boureima, I., Ramaprabhu, P. & Attal, N. 2018 Properties of the turbulent mixing layer in a spherical implosion. *J. Fluids Engng* **140**, 050905.

Brouillette, M. 2002 The Richtmyer-Meshkov instability. *Annu. Rev. Fluid Mech.* **34**, 445–468.

Chapman, P.R. & Jacobs, J.W. 2006 Experiments on the three-dimensional incompressible Richtmyer-Meshkov instability. *Phys. Fluids* **18**, 074101.

Cook, A.W., Cabot, W. & Miller, P.L. 2004 The mixing transition in Rayleigh–Taylor instability. *J. Fluid Mech.* **511**, 333–362.

Courtiaud, S., Lecysyn, N., Damamme, G., Poinsot, T. & Selle, L. 2019 Analysis of mixing in high-explosive fireballs using small-scale pressurised spheres. *Shock Waves* **29**, 339–353.

Design, R. 2008 Theory manual. Available at: chemkin/chemkin-pro.

Ding, J., Li, J., Sun, R., Zhai, Z. & Luo, X. 2019 Convergent Richtmyer-Meshkov instability of a heavy gas layer with perturbed outer interface. *J. Fluid Mech.* **878**, 277–291.

Ding, J., Si, T., Yang, J., Lu, X., Zhai, Z. & Luo, X. 2017 Measurement of a Richtmyer-Meshkov instability at an air-SF6 interface in a semiannular shock tube. *Phys. Rev. Lett.* **119**, 014501.

El Rafei, M., Flaig, M., Youngs, D.L. & Thornber, B. 2019 Three-dimensional simulations of turbulent mixing in spherical implosions. *Phys. Fluids* **31**, 114101.

Epstein, R. 2004 On the bell-plesset effects: the effects of uniform compression and geometrical convergence on the classical Rayleigh-Taylor instability. *Phys. Plasmas* **11**, 5114–5124.

Fu, Y., Yu, C. & Li, X. 2020 Energy transport characteristics of converging Richtmyer-Meshkov instability. *AIP Advances* **10**, 105302.

Groom, M. & Thornber, B. 2021 Reynolds number dependence of turbulence induced by the Richtmyer-Meshkov instability using direct numerical simulations. *J. Fluid Mech.* **908**, A31.

Hahn, M., Drikakis, D., Youngs, D., & Williams, R.J.R. 2011 Richtmyer-Meshkov turbulent mixing arising from an inclined material interface with realistic surface perturbations and reshocked flow. *Phys. Fluids* **23**, 046101.

Hill, D.L. & Abarzhi, S.I. 2020 On the dynamics of Richtmyer-Meshkov bubbles in unstable three-dimensional interfacial coherent structures with time-dependent acceleration. *Phys. Fluids* **32**, 062107.

Hosseini, S.H.R. & Takayama, K. 2005 Experimental study of Richtmyer-Meshkov instability induced by cylindrical shock waves. *Phys. Fluids* **17**, 084101.

Lei, F., Ding, J., Si, T., Zhai, Z. & Luo, X. 2017 Experimental study on a sinusoidal air/SF6 interface accelerated by a cylindrically converging shock. *J. Fluid Mech.* **826**, 819–829.

Lesieur, M. 1997 *Turbulence in Fluids*. Kluwer Academic Publishers.

LI, J., DING, J., SI, T. & LUO, X. 2020 Convergent Richtmyer-Meshkov instability of light gas layer with perturbed outer surface. *J. Fluid Mech.* **884**, R2.
LI, X., LENG, Y. & HE, Z. 2013 Optimized sixth-order monotonicity-preserving scheme by nonlinear spectral analysis. *Intl J. Numer. Meth. Fluids* **73**, 560–577.
LIANG, Y., LIU, L., ZHAI, Z., SI, T. & WEN, C. 2020*a* Evolution of shock-accelerated heavy gas layer. *J. Fluid Mech.* **886**, A7.
LIANG, Y., ZHAI, Z., DING, J. & LUO, X. 2019 Richtmyer-Meshkov instability on a quasi-single-mode interface. *J. Fluid Mech.* **872**, 729–751.
LIANG, Y., ZHAI, Z., LUO, X. & WEN, C. 2020*b* Interfacial instability at a heavy/light interface induced by rarefaction waves. *J. Fluid Mech.* **885**, A42.
LIU, W., HE, X. & YU, C. 2012 Cylindrical effects on Richtmyer-Meshkov instability for arbitrary Atwood numbers in weakly nonlinear regime. *Phys. Plasmas* **19**, 072108.
LIU, W., LI, X., YU, C., FU, Y., WANG, P., WANG, L. & YE, W. 2018 Theoretical study on finite-thickness effect on harmonics in Richtmyer-Meshkov instability for arbitrary Atwood numbers. *Phys. Plasmas* **25**, 122103.
LIU, H. & XIAO, Z. 2016 Scale-to-scale energy transfer in mixing flow induced by the Richtmyer-Meshkov instability. *Phys. Rev.* E **93**, 053112.
LIU, H., YU, B., CHEN, H., ZHANG, B., XU, H. & LIU, H. 2020 Contribution of viscosity to the circulation deposition in the Richtmyer-Meshkov instability. *J. Fluid Mech.* **895**, A10.
LIU, W., YU, C., YE, W., WANG, L. & HE, X. 2014 Nonlinear theory of classical cylindrical Richtmyer-Meshkov instability for arbitrary Atwood numbers. *Phys. Plasmas* **21**, 062119.
LIVESCU, D. 2020 Turbulence with large thermal and compositional density variations. *Annu. Rev. Fluid Mech.* **52**, 309–341.
LOMBARDINI, M. 2008 Richtmyer-Meshkov instability in converging geometries. Ph.D. thesis, California Institute of Technology.
LOMBARDINI, M. & PULLIN, D.I. 2009 Small-amplitude perturbations in the three-dimensional cylindrical Richtmyer-Meshkov instability. *Phys. Fluids* **21**, 114103.
LOMBARDINI, M., PULLIN, D.I. & MEIRON, D.I. 2014*a* Turbulent mixing driven by spherical implosions. Part 1. Flow description and mixing-layer growth. *J. Fluid Mech.* **748**, 85–112.
LOMBARDINI, M., PULLIN, D.I. & MEIRON, D.I. 2014*b* Turbulent mixing driven by spherical implosions. Part 2. Turbulence statistics. *J. Fluid Mech.* **748**, 113–142.
LUO, X., DING, J., WANG, M., ZHAI, Z. & SI, T. 2015 A semi-annular shock tube for studying cylindrically converging Richtmyer-Meshkov instability. *Phys. Fluids* **27**, 091702.
LUO, X., LI, M., DING, J., ZHAI, Z. & SI, T. 2019*a* Nonlinear behaviour of convergent Richtmyer-Meshkov instability. *J. Fluid Mech.* **877**, 130–141.
LUO, X., LIANG, Y., SI, T. & ZHAI, Z. 2019*b* Effects of non-periodic portions of interface on Richtmyer-Meshkov instability. *J. Fluid Mech.* **861**, 309–327.
LUO, X., ZHANG, F., DING, J., SI, T., YANG, J., ZHAI, Z. & WEN, C. 2018 Long-term effect of Rayleigh-Taylor stabilization on converging Richtmyer-Meshkov instability. *J. Fluid Mech.* **849**, 231–244.
MARKSTEIN, G.H. 1957 Flow disturbances induced near a slightly wavy contact surface, or flame front, traversed by a shock wave. *J. Aerosp. Sci.* **24**, 238–239.
MESHKOV, E.E. 1969 Instability of the interface of two gases accelerated by a shock wave. *Sov. Fluid Dyn.* **4** (5), 101–104.
MIKAELIAN, K.O. 1990 Rayleigh-Taylor and Richtmyer-Meshkov instabilities and mixing in stratified spherical shells. *Phys. Rev.* A **42**, 3400–3420.
MIKAELIAN, K.O. 2005 Rayleigh-Taylor and Richtmyer-Meshkov instabilities and mixing in stratified cylindrical shells. *Phys. Fluids* **17**, 094105.
MOHAGHAR, M., CARTER, J., MUSCI, B., REILLY, D., MCFARLAND, J. & RANJAN, D. 2017 Evaluation of turbulent mixing transition in a shock-driven variable-density flow. *J. Fluid Mech.* **831**, 779–825.
MORGAN, B.E. & WICKETT, M.E. 2015 Three-equation model for the self-similar growth of Rayleigh-Taylor and Richtmyer-Meskov instabilities. *Phys. Rev.* E **91**, 043002.
PENG, N., YANG, Y., WU, J. & XIAO, Z. 2021 Mechanism and modelling of the secondary baroclinic vorticity in the Richtmyer–Meshkov instability. *J. Fluid Mech.* **911**, A56.
PLESSET, M.S. 1954 On the stability of fluid flows with spherical symmetry. *J. Appl. Phys.* **25**, 96–98.
RAYLEIGH, LORD 1883 Investigation of the character of the equilibrium of an incompressible heavy fluid of variable density. *Proc. Lond. Math. Soc.* **14**, 170–177.
REESE, D.T., AMES, A.M., NOBLE, C.D., OAKLEY, J.G., RATHAMER, D.A. & BONAZZA, R. 2018 Simultaneous direct measurements of concentration and velocity in the Richtmyer-Meshkov instability. *J. Fluid Mech.* **849**, 541–575.

RICHTMYER, R.D. 1960 Taylor instability in shock acceleration of compressible fluids. *Commun. Pure Appl. Maths* **13**, 297–319.

RODRIGUEZ, V., SAUREL, R., JOURDAN, G. & HOUAS, L. 2017 Impulsive dispersion of a granular layer by a weak blast wave. *Shock Waves* **27**, 187–198.

SUN, P., DING, J., HUANG, S., LUO, X. & CHENG, W. 2020*a* Microscopic Richtmyer-Meshkov instability under strong shock. *Phys. Fluids* **32**, 024109.

SUN, R., DING, J., ZHAI, Z., SI, T. & LUO, X. 2020*b* Convergent RichtmyerMeshkov instability of heavy gas layer with perturbed inner surface. *J. Fluid Mech.* **902**, A3.

TANG, J., ZHANG, F., LUO, X. & ZHAI, Z. 2021 Effect of Atwood number on convergent Richtmyer–Meshkov. *Acta Mechanica Sin.* **37**, 434–446.

TAYLOR, G.I. 1950 The instability of liquid surfaces when accelerated in a direction perpendicular to their planes. I. *Proc. R. Soc. Lond.* A **201**, 192–196.

TRITSCHLER, V.K., ZUBEL, M., HICKEL, S. & ADAMS, N.A. 2014 Evolution of length scales and statistics of Richtmyer-Meshkov instability from direct numerical simulations. *Phys. Rev.* E **90**, 063001.

VANDENBOOMGAERDE, M., ROUZIER, P., SOUFFLAND, D., BIAMINO, L., JOURDAN, G., HOUAS, L. & MARIANI, C. 2018 Nonlinear growth of the converging Richtmyer-Meshkov instability in a conventional shock tube. *Phys. Rev. Fluids* **3**, 014001.

WILKE, C.R. 1950 A viscosity equation for gas mixtures. *J. Chem. Phys.* **18**, 517–519.

YOUNGS, D.L. 1991 Three-dimensional numerical simulation of turbulent mixing by Rayleigh-Taylor instability. *Phys. Fluids* A *Fluid Dyn.* **3**, 1312.

YOUNGS, D.L. 1994 Numerical simulation of mixing by Rayleigh-Taylor and Richtmyer-Meshkov instabilities. *Laser Part. Beams* **12**, 725–750.

YOUNGS, D.L. & WILLIAMS, R.J.R. 2008 Turbulent mixing in spherical implosions. *Intl J. Numer. Meth. Fluids* **56**, 1597–1603.

YU, C., HONG, R., XIAO, Z. & CHEN, S. 2013 Subgrid-scale eddy viscosity model for helical turbulence. *Phys. Fluids* **25**, 095101.

ZHAI, Z., LI, W., SI, T., LUO, X., YANG, J. & LU, X. 2017 Refraction of cylindrical converging shock wave at an air/helium gaseous interface. *Phys. Fluids* **29**, 016102.

ZHAI, Z., ZHANG, F., ZHOU, Z., DING, J. & WEN, C. 2019 Numerical study on Rayleigh-Taylor effect on cylindrically converging Richtmyer-Meshkov instability. *Sci. China-Phys. Mech. Astron.* **62**, 124712.

ZHANG, Y., NI, W., RUAN, Y. & XIE, H. 2020*a* Quantifying mixing of Rayleigh-Taylor turbulence. *Phys. Rev. Fluids* **5**, 104501.

ZHANG, Y., RUAN, Y., XIE, H. & TIAN, B. 2020*b* Mixed mass of classical Rayleigh-Taylor mixing at arbitrary density ratios. *Phys. Fluids* **32**, 011702.

ZHAO, Y., XIA, M. & CAO, Y. 2020 A study of bubble growth in the compressible Rayleigh-Taylor and Richtmyer-Meshkov instabilities. *AIP Advances* **10**, 015056.

ZHOU, Y. 2017*a* Rayleigh–Taylor and Richtmyer-Meshkov instability induced flow, turbulence, and mixing. I. *Phys. Rep.* **720–722**, 1–136.

ZHOU, Y. 2017*b* Rayleigh–Taylor and Richtmyer-Meshkov instability induced flow, turbulence, and mixing. II. *Phys. Rep.* **723–725**, 1–160.

ZHOU, Y., CABOT, W.H. & THORNBER, B. 2016 Asymptotic behavior of the mixed mass in Rayleigh-Taylor and Richtmyer-Meshkov instability induced flows. *Phys. Plasmas* **23**, 052712.

ZHOU, Y., CLARK, T.T., CLARK, D.S. & GLENDINNING, S.G. 2019 Turbulent mixing and transition criteria of flows induced by hydrodynamic instabilities. *Phys. Plasmas* **26**, 080901.

ZHOU, Y., WILLIAMS, R.J.R., RAMAPRABHU, P., *et al.* 2021 Rayleigh-Taylor and Richtmyer-Meshkov instabilities: a journey through scales. *Physica* D **423**, 132838.

ZOU, L., AL-MAROUF, M., CHENG, W., SAMTANEY, R., DING, J. & LUO, X. 2019 Richtmyer-Meshkov instability of an unperturbed interface subjected to a diffracted convergent shock. *J. Fluid Mech.* **879**, 448–467.